

THE MOLECULAR GAS ENVIRONMENT IN THE 20 KMS⁻¹ CLOUD IN THE CENTRAL MOLECULAR ZONE

XING LU^{1,2,3}, QIZHOU ZHANG³, JENS KAUFFMANN⁴, THUSHARA PILLAI⁴, STEVEN N. LONGMORE⁵, J. M. DIEDERIK KRUIJSSSEN⁶, CARA BATTERSBY³, HAUYU BAOBAB LIU⁷, ADAM GINSBURG⁸, ELISABETH A. C. MILLS⁹, ZHI-YU ZHANG^{10,7}, AND QIUSHENG GU¹

¹School of Astronomy and Space Science, Nanjing University, Nanjing, Jiangsu 210093, China; xinglv.nju@gmail.com

²National Astronomical Observatory of Japan, 2-21-1 Osawa, Mitaka, Tokyo, 181-8588, Japan

³Harvard-Smithsonian Center for Astrophysics, 60 Garden Street, Cambridge, MA 02138, USA

⁴Max Planck Institut für Radioastronomie, Auf dem Hügel 69, D-53121 Bonn, Germany

⁵Astrophysics Research Institute, Liverpool John Moores University, 146 Brownlow Hill, Liverpool L3 5RF, UK

⁶Astronomisches Rechen-Institut, Zentrum für Astronomie der Universität Heidelberg, Mönchhofstraße 12-14, 69120 Heidelberg, Germany

⁷European Southern Observatory, Karl-Schwarzschild-Str. 2, D-85748 Garching, Germany

⁸National Radio Astronomy Observatory, Socorro, NM 87801, USA

⁹Department of Physics and Astronomy, San Jose State University, One Washington Square, San Jose, CA 95192, USA

¹⁰Institute for Astronomy, University of Edinburgh, Royal Observatory, Blackford Hill, Edinburgh EH9 3HJ

ABSTRACT

We recently reported a population of protostellar candidates in the 20 km s⁻¹ cloud in the Central Molecular Zone of the Milky Way, traced by H₂O masers in gravitationally bound dense cores. In this paper, we report high-angular-resolution ($\sim 3''$) molecular line studies of the environment of star formation in this cloud. Maps of various molecular line transitions as well as the continuum at 1.3 mm are obtained using the Submillimeter Array. Five NH₃ inversion lines and the 1.3 cm continuum are observed with the Karl G. Jansky Very Large Array. The interferometric observations are complemented with single-dish data. We find that the CH₃OH, SO, and HNCO lines, which are usually shock tracers, are better correlated spatially with the compact dust emission from dense cores among the detected lines. These lines also show enhancement in intensities with respect to SiO intensities toward the compact dust emission, suggesting the presence of slow shocks or hot cores in these regions. We find gas temperatures of $\gtrsim 100$ K at 0.1-pc scales based on RADEX modelling of the H₂CO and NH₃ lines. Although no strong correlations between temperatures and linewidths/H₂O maser luminosities are found, in high-angular-resolution maps we notice several candidate shock heated regions offset from any dense cores, as well as signatures of localized heating by protostars in several dense cores. Our findings suggest that at 0.1-pc scales in this cloud star formation and strong turbulence may together affect the chemistry and temperature of the molecular gas.

Keywords: ISM: clouds — stars: formation — Galaxy: center

1. INTRODUCTION

The Central Molecular Zone (CMZ) is the inner ~ 500 pc of the Galaxy (Morris & Serabyn 1996) and contains more than $10^7 M_{\odot}$ of dense molecular gas (mean density in clouds \sim a few 10^3 cm⁻³; Ferrière et al. 2007). Within the CMZ are a series of massive molecular clouds with typical projected scales of 10 pc and masses of $10^5 M_{\odot}$. These clouds are characterized by large turbulent linewidths (FWHM ~ 10 – 10^2 km s⁻¹; Shetty et al. 2012; Kruijssen & Longmore 2013). Spectral line studies using single-dish observations have found interesting gas properties related to such strong turbulence. Mappings of shock

tracers, such as SiO, revealed that their emission is widespread but non-uniform, suggesting large-scale shocks at $\gtrsim 1$ -pc scales (Martín-Pintado et al. 1997; Riquelme et al. 2010; Jones et al. 2012). Widespread emission of organic molecules has been detected and these molecules are suggested to be released from grain mantles by shocks (Martín-Pintado et al. 2001; Requena-Torres et al. 2006, 2008). In addition, efforts have been made to map gas temperatures in the CMZ using multiple transitions of NH₃ or H₂CO, which have revealed ubiquitously high temperatures (50–100 K or higher) at $\gtrsim 1$ -pc scales and suggested that turbulent shocks could be the heating source (Mills & Morris

2013; Ao et al. 2013; Ginsburg et al. 2016; Immer et al. 2016). These studies indicate that strong turbulence plays a vital role in shaping the molecular gas environment in the CMZ clouds at >1 -pc scales, though the origin of the turbulence is under debate (e.g., Rodríguez-Fernández et al. 2006; Kruijssen et al. 2015).

However, an ambiguity exists in single-dish observations that use linewidths to indicate turbulent strength: at angular resolutions of $\sim 30''$ (1 pc at the distance of the CMZ) and above, linewidths may have contributions from unresolved systematic motions (e.g., rotation, infall) thus may be questionable to be a good indicator of turbulence (e.g., discussions in Henshaw et al. 2016). Higher angular resolutions of $3''$ (0.1 pc) would help to resolve systematic motions of dense cores within clouds in order to evaluate the impact of turbulence on gas.

Star formation is one of the key factors in shaping the gas environment in galaxies (Kennicutt & Evans 2012). Active star formation can reveal itself by heating the ambient gas (e.g., hot molecular cores, Araya et al. 2005) as well as changing the chemical composition of gas (e.g., enhancement of SiO emission by outflows, Garay et al. 2000). However, it remains unclear whether star formation has a major impact on the molecular gas in addition to strong turbulence in the CMZ clouds. The overall star formation rate (SFR) in the CMZ measured with infrared luminosities is ~ 0.05 – $0.15 M_{\odot} \text{ yr}^{-1}$ (Barnes et al. 2017), which is significantly lower than expected from the well-established correlation between amount of dense gas and star formation (Longmore et al. 2013), e.g., the Kennicutt-Schmidt relations (Kennicutt 1998; Kennicutt & Evans 2012). Kruijssen et al. (2014) discussed mechanisms that may explain the currently low SFR in the CMZ, including strong turbulence, high virial ratios, acoustic instabilities, and episodic cycling. They present a self-consistent scenario in which star formation in the CMZ may proceed episodically, regulated by turbulence driving and feedback. This idea was quantified by Krumholz & Kruijssen (2015) and Krumholz et al. (2017), who showed that the combination of these mechanisms implies that a wide range of star-forming environments should be present within the CMZ, with widely varying degrees of star formation activity.

Except for a few active star forming regions such as Sgr B2, most of the clouds in the CMZ have been found to be relatively quiescent in star formation (Guesten & Downes 1983; Lis et al. 1994; Immer et al. 2012; Kauffmann et al. 2016). An example is G0.253+0.016, which shows quite inactive star formation (e.g., a weak H₂O maser, Lis et al. 1994; a likely gravitationally bound dense core, Kauffmann et al. 2013; Johnston et al. 2014; Rathborne et al. 2014b; and no evidence of free-free emission from H II regions,

Rodríguez & Zapata 2013; Mills et al. 2015). Observations of spectral lines show that the gas in G0.253+0.016 is dominantly influenced by strong turbulence (Rathborne et al. 2014a, 2015), but little evidence of being affected by star formation has been found. In other CMZ clouds, to what extent star formation can affect the environment remains to be answered, and observations with angular resolutions of $\lesssim 3''$ (0.1 pc) are required to match with the scale of dense cores where star formation takes place ($\lesssim 0.1$ pc; Kauffmann et al. 2008; Lu et al. 2014).

Therefore, to examine the impact of turbulence and star formation on the molecular gas environment in CMZ clouds, interferometric observations that can provide $\sim 3''$ or better angular resolutions are necessary. We also need an optimized sample for our study, e.g., a CMZ cloud with more active star formation than G0.253+0.016.

In our recent work (Lu et al. 2015), we studied star formation in the 20 km s^{-1} cloud, a massive ($\gtrsim 10^5 M_{\odot}$) molecular cloud in the Sgr A complex (Ferrière 2012). Single-dish observations have found this cloud to be extremely turbulent with linewidth of $\gtrsim 10 \text{ km s}^{-1}$ at 1-pc scales and large velocity gradient of 2 – $5 \text{ km s}^{-1} \text{ pc}^{-1}$ along its major axis (Coil & Ho 1999; Tsuboi et al. 2011). In Lu et al. (2015), we detected 18 H₂O masers and associated dense cores in this cloud, thus revealing a population of deeply embedded protostellar candidates. Therefore, with both strong turbulence and relatively active star formation activity, the 20 km s^{-1} cloud is an appropriate sample for understanding the interplay between star formation and the environmental molecular gas.

Here we continue to use high-angular-resolution interferometric observations of molecular lines to study the molecular gas environment in the 20 km s^{-1} cloud. We use a number of molecular lines at 1.3 mm wavelengths including both dense gas tracers (e.g., H₂CO) and shock tracers (e.g., SiO), and five NH₃ lines at 1.3 cm wavelengths (K band) that are conventional dense gas tracers. Moreover, multiple transitions of H₂CO and NH₃ can be used as thermometers to reveal impact of star formation and turbulence on gas temperatures, in which the two lines may trace different gas components, in terms of chemistry and/or density, thus complement each other. In Section 2, we outline our interferometric and single-dish observations as well as archival data used in this paper. In Section 3, we present the results, including the 1.3 mm continuum and spectral lines, the 1.3 cm continuum, the NH₃ lines, and gas temperatures derived from H₂CO and NH₃. In Section 4, we focus on two points: the impact of star formation and turbulence on the chemical composition of gas (spatial correlations between dust and spectral line emission, enhancement of

emission of shock tracers), and the heating of gas at 0.1-pc scales by star formation and turbulence. We draw our conclusions and summarize our results in Section 5. In this paper we adopt the distance to the Galactic Center of 8.34 kpc (Reid et al. 2014).

2. OBSERVATIONS AND DATA REDUCTION

2.1. Submillimeter Array (SMA) Observations

We observed eight positions as a mosaic in the 20 km s^{-1} cloud in 2013 with the SMA¹¹ (Ho et al. 2004) at 1.3 mm wavelengths in the compact and subcompact configurations. Spectral lines between 216.9–220.9 GHz and 228.9–232.9 GHz as well as the continuum were obtained at the same time. Details of the SMA observations and data reduction, using the IDL supersets MIR¹², MIRIAD (Sault et al. 1995), and CASA (McMullin et al. 2007), have been reported in Lu et al. (2015). In the end we obtained image cubes of molecular lines, with typical clean beams of $5''.0 \times 2''.8$ at position angles of 5° , and rms of $0.11\text{--}0.14 \text{ Jy beam}^{-1}$ per 1.1 km s^{-1} velocity bin. In Section 2.6, we will discuss the combination of the SMA and single-dish data.

2.2. Karl G. Jansky Very Large Array (VLA) Observations

We observed three positions as a mosaic in the 20 km s^{-1} cloud in 2013 with the National Radio Astronomy Observatory (NRAO¹³) VLA at K band in the DnC configuration. The H_2O maser transition at 22.2 GHz, five NH_3 inversion transitions from $(J, K)=(1, 1)$ to $(5, 5)$, two CCS lines and one NH_2D line, as well as the continuum using a total bandwidth of 1 GHz were observed. Details of the VLA observations and reduction of the H_2O maser and continuum data, using CASA, have been reported in Lu et al. (2015). The CCS and NH_2D lines were not detected at a sensitivity of $2.0 \text{ mJy per } 3'' \times 2'' \text{ beam per } 1 \text{ km s}^{-1}$.

For the NH_3 (1, 1) and (2, 2) transitions, the 16-MHz-wide subbands were split into 1024 channels, leading to a velocity coverage of 200 km s^{-1} and a channel width of 0.2 km s^{-1} , which can cover all the hyperfine splittings of these two transitions. For NH_3 (3, 3) to (5, 5), the satellite components of the hyperfine splittings are usually much weaker, therefore the 8-MHz-wide subbands, split into 512 channels, were used to cover the main com-

ponents only, with a velocity coverage of 100 km s^{-1} and a channel width of 0.2 km s^{-1} . To increase the signal-to-noise ratios, we regridded the visibility data to a velocity bin of 1 km s^{-1} before CLEANing.

Then we imaged the NH_3 data with CASA 4.5.0. From the early versions of the CLEANed images, we noticed that the emission of NH_3 , especially that of NH_3 (3, 3), is extended in nature, thus the canonical CLEAN with pixel-by-pixel clean component finding algorithm did not recover such emission well. This is evidenced by the extended ‘stripes’ and strong ‘negative bowls’ seen in the images. Therefore, we used the multi-scale CLEAN in CASA, which implements multi-scale clean component finding algorithm, to improve the imaging of extended structures. We used multi-scale parameters of 0, 5, 20, and 80 pixels, corresponding to angular scales of $0''$, $3''$, $12''$, and $48''$. The stripes and negative bowls are significantly suppressed in the obtained images. Typical rms of the images is $1.8\text{--}2.0 \text{ mJy beam}^{-1}$ per 1 km s^{-1} velocity bin, with beams of $3''.0 \times 2''.1$ at position angles of 10° . In Section 2.6, we will discuss the combination of the VLA and single-dish NH_3 data. Similarly, we reprocessed the VLA 1.3 cm continuum data that also present extended structures with multi-scale CLEAN.

2.3. Caltech Submillimeter Observatory (CSO) Heterodyne Observations

In April 2014, we observed a $2''.5 \times 4''.0$ area in the 20 km s^{-1} cloud in the on-the-fly position switching mode with the CSO. The heterodyne receiver was tuned to cover the same frequency range of the SMA observations in the double-sideband mode. The wideband Fast Fourier Transform Spectrometer (FFTS2) and the Fast Fourier Transform Spectrometer (FFTS1) backends were connected to the receiver in parallel. The FFTS2 was used to cover 228.9–232.9 GHz, which in the double-sideband mode also sampled 216.9–220.9 GHz. The channel width is $\sim 0.27 \text{ MHz}$, corresponding to $\sim 0.35 \text{ km s}^{-1}$ at 230 GHz. The FFTS1 was used to cover 231.9–232.9 GHz as well as 216.9–217.9 GHz in the double-sideband mode, in order to observe the SiO 5–4 line at $\sim 217.1 \text{ GHz}$ with a finer channel width of $\sim 0.12 \text{ MHz}$ than the FFTS2, corresponding to $\sim 0.16 \text{ km s}^{-1}$ at 230 GHz. However the FFTS2 data are adequate for our purpose hence the FFTS1 data are not used in this paper. The on-the-fly mapping was done in two orthogonal directions, between which we shifted the IF frequency by 50 MHz to separate spectral lines from the two sidebands. The optical depth at 225 GHz relative to zenith during the observation was 0.07–0.10, corresponding to precipitable water vapor of 1.3–2.0 mm. The system temperature of FFTS2 was 250–300 K during the observation. We derived a beam efficiency of 0.66 by observing Mars.

¹¹ The Submillimeter Array is a joint project between the Smithsonian Astrophysical Observatory and the Academia Sinica Institute of Astronomy and Astrophysics, and is funded by the Smithsonian Institution and the Academia Sinica.

¹² <https://www.cfa.harvard.edu/~cqi/mircook.html>

¹³ The National Radio Astronomy Observatory is a facility of the National Science Foundation operated under cooperative agreement by Associated Universities, Inc.

There is an atmospheric feature, probably a H_2O absorption line, at ~ 231.3 GHz, corresponding to ~ 218.6 GHz in the lower-sideband with the double-sideband mode. The full width at zero intensity of the feature is 0.3–0.4 GHz, depending on the choice of the continuum baseline. Therefore, two H_2CO lines ($3_{2,2}-2_{2,1}$ and $3_{2,1}-2_{2,0}$), the CH_3OH $4_{2,2}-3_{1,0}$ line, and possibly the HC_3N 24–23 line (cf. Figure 2) were affected. All other lines detected by the CSO were free from atmospheric contamination or double-sideband confusion. We processed the data with the CLASS package¹⁴ and obtained the final images after a baseline subtraction and a correction for the beam efficiency.

2.4. Archival Atacama Pathfinder EXperiment (APEX) Heterodyne and Bolocam Galactic Plane Survey (BGPS) Data

We used spectral line data from APEX at 218–219 GHz that cover the three H_2CO lines as well as the HC_3N and CH_3OH lines, which were released by Ginsburg et al. (2016). These data readily complement our CSO heterodyne data that missed this frequency range due to the atmospheric contamination.

The 1.1 mm continuum data were obtained from the BGPS v2.1 (Ginsburg et al. 2013). The intensities were multiplied by a factor of 0.5 to convert to those at 1.33 mm (equivalent to the IF frequency of the SMA observations, 225 GHz) for the use of data combination, assuming a dust emissivity index of 2 (Walker et al., in prep.).

2.5. Green Bank Telescope (GBT) NH_3 Data

We used the NH_3 inversion lines from $(J, K)=(1, 1)$ to $(5, 5)$ from the NRAO GBT observations (PI: H. B. Liu). The observations were done on November 7, 2011. The $(J, K)=(3, 3)$ to $(5, 5)$ data have been published in Minh et al. (2013) and details of the observations can be found therein. The GBT observations fully cover the VLA mosaic field hence can be combined with the latter to recover diffuse NH_3 emission.

2.6. Combination of the Interferometer and Single-Dish Data

In order to recover the missing fluxes in the interferometric observations, we combined the SMA and VLA data with single-dish data from CSO, APEX or GBT, using the *feather* task in CASA.

First, we combined the SMA 1.3 mm continuum data and the BGPS data. We weighted the BGPS image with the primary beams of the SMA, to suppress the signal outside of the SMA primary beams. Then we

used the *feather* task to combine the two datasets, with a lowpass filtering at a spatial scale of 10 m (corresponding to an angular scale of $36''$ at the wavelength of 1.33 mm) for the BGPS data to filter out the high spatial frequency data¹⁵. At last we compared the fluxes of the combined image and the BGPS image to check the consistency. The difference between total fluxes within the FWHM of the SMA primary beams (see the dotted loop in Figure 1) for the combined image and the BGPS image (weighted by the SMA primary beams) is 1.6%, which we considered to be acceptable. The results are presented in Section 3.1.

Similarly, we combined the SMA and single-dish spectral line data. For several spectral lines around 218.6 GHz, including H_2CO $3_{2,2}-2_{2,1}$ and $3_{2,1}-2_{2,0}$, CH_3OH $4_{2,2}-3_{1,0}$, and HC_3N 24–23, the CSO data were affected by an atmospheric feature, therefore we used the APEX data which are free from contamination. The H_2CO $3_{0,3}-2_{0,2}$ line in the CSO data was not affected by the atmospheric feature. However, later in Section 3.5 we will use line ratios of H_2CO to derive gas temperatures. To avoid any offset between H_2CO images, we made combined images with the APEX data also for H_2CO $3_{0,3}-2_{0,2}$. For the other lines we used the CSO data. We first weighted the single-dish images with the primary beams of the SMA, then combined them with the SMA images using the *feather* task with a lowpass filtering of spatial scales at 10 m ($36''$ at the wavelength of 1.33 mm) for the CSO data or 12 m ($31''$ at the wavelength of 1.33 mm) for the APEX data.

The VLA and GBT NH_3 data were combined following the same procedures. The *feather* task was run with a lowpass filtering of spatial scales at 100 m ($36''$ at the wavelength of 1.3 cm) for the GBT data.

All the combined images processed above have been convolved with primary beams of the interferometers. We also applied primary-beam corrections to them to obtain correct fluxes. In the following sections, we identified structures using the combined images and measured fluxes using the primary-beam corrected images.

3. RESULTS

3.1. SMA+BGPS Dust Emission

In Lu et al. (2015), we reported the discovery of 17 dense cores traced by the SMA 1.3 mm continuum emis-

¹⁵ In principle we should use a lowpass filtering at 12 m ($31''$ at the wavelength of 1.33 mm), which provides the same spatial frequency as the original BGPS data with a 10-m dish at the wavelength of 1.1 mm. However due to the limitation of the *feather* task we are unable to set such a large parameter. Using 10 m is more aggressive for filtering high spatial frequency data. We have confirmed that varying the lowpass filtering parameters does not affect the resulting image (variation in total fluxes $< 1\%$, variation in intensities $< 1/3$ of the rms).

¹⁴ <http://www.iram.fr/IRAMFR/GILDAS>

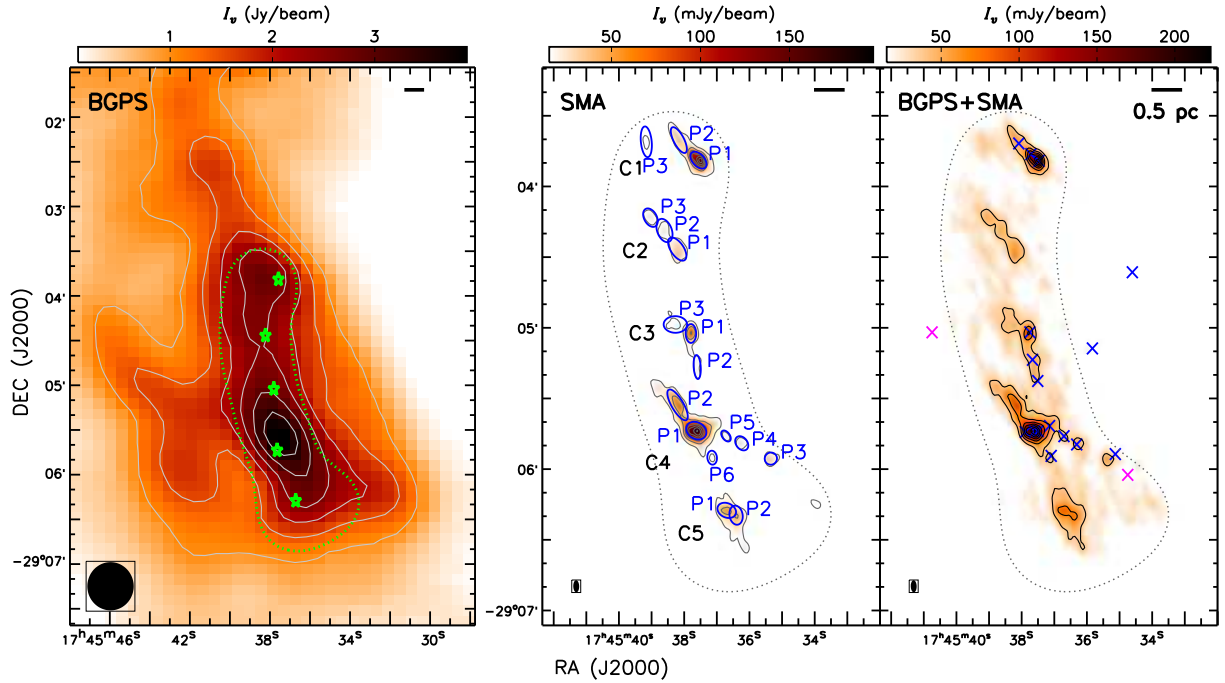


Figure 1. 1.3 mm continuum maps of 20 km s^{-1} cloud. Left: BGPS continuum map, which has been multiplied by factor 0.5 to convert to intensities at the frequency of the SMA observations, is shown in the background image, with contours at 1.0–3.5 Jy beam^{-1} in steps of 0.5 Jy beam^{-1} . The blue dotted loop shows the FWHM of the SMA primary-beams. The 33'' effective resolution of the BGPS is shown in the lower left corner. Stars mark the most massive dense cores in each of the five clumps (all named as ‘P1’ in the middle panel). Middle: both contours and image show the SMA 1.3 mm continuum emission (not corrected for primary beam responses in order to have a uniform rms). The contours are between 5σ and 65σ levels in steps of 10σ , where $1\sigma=3 \text{ mJy beam}^{-1}$. The dotted loop shows the FWHM of the SMA primary beams. The synthesized beam of the SMA, $5''.0 \times 2''.8$ with a position angle of 5° , is shown in the lower left corner. The five clumps, from C1 to C5, are labeled. The blue ellipses are the results of Gaussian fittings to dense cores. Right: both contours and image show the SMA+BGPS combined 1.3 mm continuum emission. The contours levels are selected at $24 \text{ mJy beam}^{-1} + 3 \text{ mJy beam}^{-1} \times [5, 15, 25, 35, 45, 55, 65]$, in order to highlight the similarity with the middle panel at 0.1-pc scales. The H_2O masers detected by the VLA are marked by crosses, with magenta ones showing cataloged AGB stars (Lu et al. 2015).

sion. Here we use the combined SMA and BGPS continuum data to trace the diffuse dust emission in the cloud. Later in Section 4.1 we will use the SMA-only data and the combined SMA+BGPS data to represent compact and diffuse dust emission, respectively.

The BGPS map, the continuum image made with the SMA data, and that made with the combined SMA+BGPS data are shown in Figure 1. The total 1.3 mm continuum flux, within the FWHM of the SMA primary beams, estimated from the primary-beam-corrected SMA+BGPS image, is 19.2 Jy. The 1.3 cm continuum flux in the same area observed by the VLA is ~ 0.4 Jy (Lu et al. 2015). There is no evidence of any optically thick free-free emission in the area at the considered frequencies. Assuming a completely flat spectral index from 1.3 cm to shorter wavelengths, the flux of 0.4 Jy does not make significant difference to the total flux at 1.3 mm. Therefore, we conclude that the 1.3 mm continuum is dominated by dust emission.

The dust emission maps in Figure 1 demonstrate that the SMA observations are able to resolve dense cores at 0.1-pc scales. Therefore, in the following we will use

them as well as VLA observations that have an even higher angular resolution to study the gas environment of star formation in the 20 km s^{-1} cloud.

3.2. SMA+CSO/APEX 1.3 mm Spectral Lines

The SMA, CSO, and APEX observations detected a number of molecular lines in the 20 km s^{-1} cloud. In Figure 2, spectra of the full SMA 8 GHz band are presented for the most massive dense cores in each of the five clumps. The detected spectral lines in general can be classified into several groups based on their excitation conditions (e.g., critical densities¹⁶): ^{12}CO and ^{13}CO 2–1 lines have low critical densities (10^2 – 10^3 cm^{-3}) and become optically thick quickly, therefore are usually diffuse gas tracers; H_2CO , HC_3N , HNC , CH_3OH ,

¹⁶ The critical density, assuming optically thin and without a background, is the density for which the net radiative decay rate from the upper level to the lower level equals the rate of collisional depopulation out of the upper level for a multilevel system (Shirley 2015). A temperature of 100 K is assumed when calculating critical densities in this section.

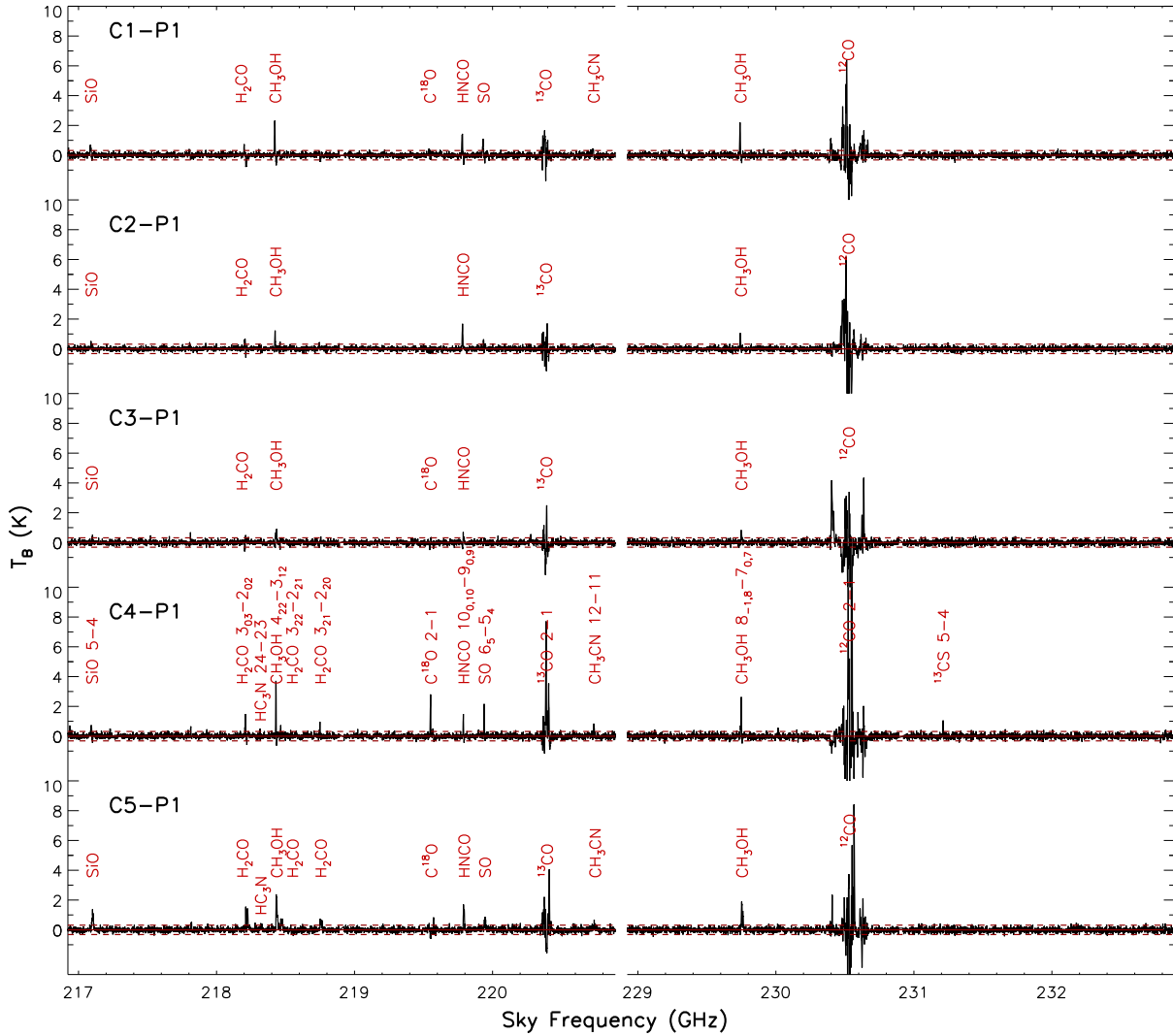


Figure 2. Spectral lines detected by the SMA toward the most massive dense cores in each of the five clumps. Names of molecular species are marked; for C4-P1 where all the species are detected, transitions are also labeled. Horizontal dashed lines in each spectrum mark the $\pm 3\sigma$ levels. For ^{12}CO and ^{13}CO lines, absorption features can be clearly seen.

CH_3CN , and ^{13}CS transitions have high critical densities ($10^5\text{--}10^6\text{ cm}^{-3}$) and are usually dense gas tracers; SiO, HNCO, SO, and CH_3OH molecules are usually released to gas phase from dust by shocks hence their lines are usually shock tracers, though they may not uniquely trace shocks in the CMZ.

The integrated intensities over velocities, represented by the zeroth moment maps, of all the lines detected in the SMA observations are shown in Figures 3. Except otherwise noted, we integrated over V_{LSR} between -20 and 40 km s^{-1} , and discarded pixels below 5σ in the datacubes when making the moment maps. For the ^{13}CO line that is broad in velocity, we integrated between -40 and 60 km s^{-1} . For the $\text{H}_2\text{CO } 3_{2,2}\text{--}2_{2,1}$ and $\text{CH}_3\text{OH } 4_{2,2}\text{--}3_{1,2}$ lines that are blended with each other along several lines of sight, we integrated them between -20 and 28 km s^{-1} , and between -15 and 40 km s^{-1} , re-

spectively, to avoid blending. In the following we discuss these lines by groups.

3.2.1. Diffuse Gas Tracers

^{12}CO and $^{13}\text{CO } 2\text{--}1$ in 20 km s^{-1} cloud spread diffusely, in both emission and absorption. They are both extended beyond the mapped area according to single-dish observations (e.g., Oka et al. 1998, 2012), hence image fidelity may suffer from strong side-lobes from emission outside of the region, even after combining with single-dish data. We attempted to search for signatures of bipolar outflows traced by ^{12}CO or ^{13}CO emission, but was unable to confirm any due to the complex kinematics. Therefore, we only show an integrated intensity map of $^{13}\text{CO } 2\text{--}1$ in Figure 3 and proceed to discuss the other lines.

$\text{C}^{18}\text{O } 2\text{--}1$ does not show absorption features and its emission is less extended, as shown in Figure 3. We will

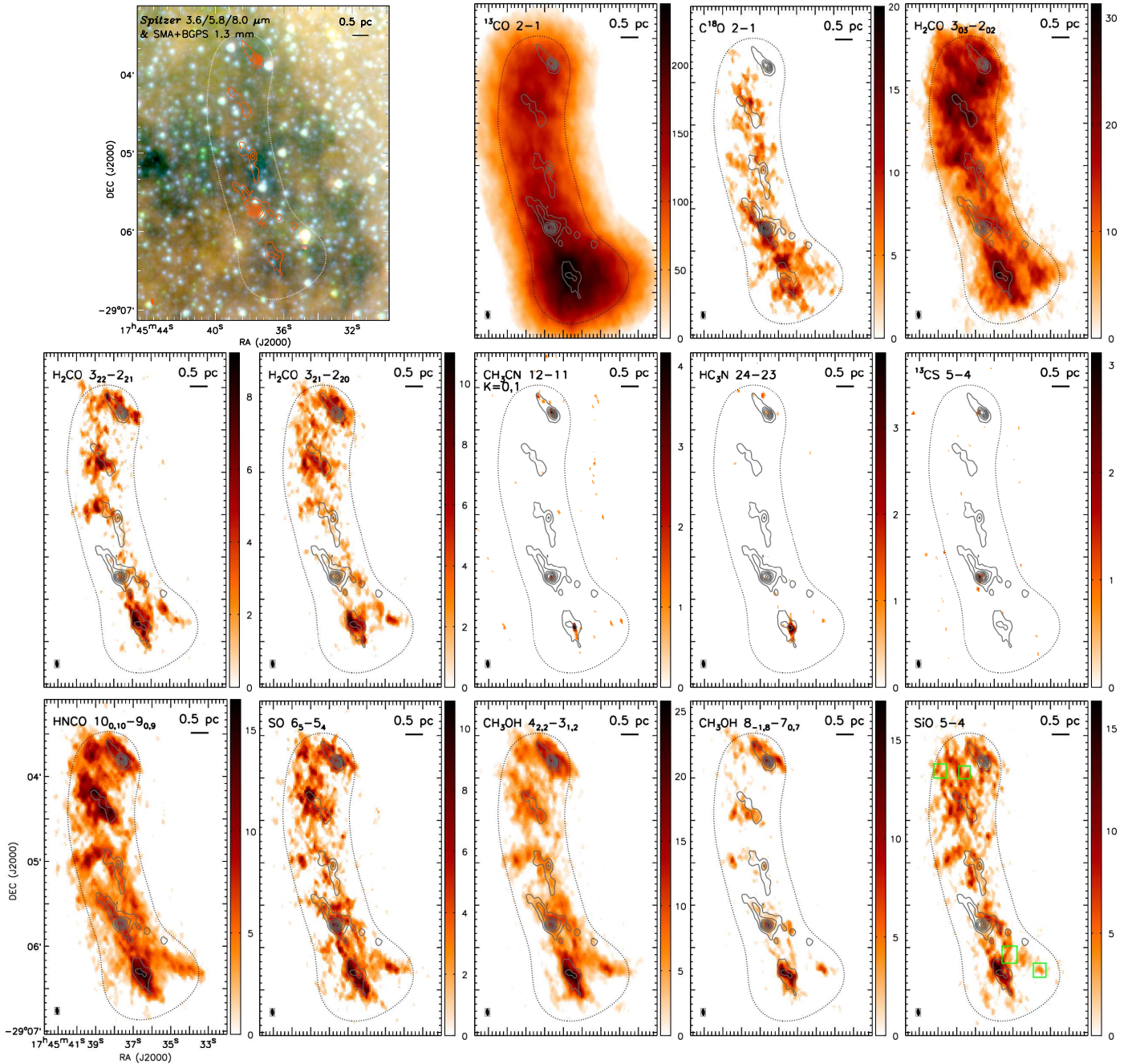


Figure 3. The first panel shows a three-color image at $3.6 \mu\text{m}$, $5.8 \mu\text{m}$, and $8.0 \mu\text{m}$ from the *Spitzer* Space Telescope/IRAC (Stolovy et al. 2006). All the other panels show the integrated intensity maps (not corrected for primary beam responses in order to have a uniform rms) of the lines detected in the SMA+CSO/APEX observations (except ^{13}CS which includes only the SMA observation), in unit of $\text{Jy beam}^{-1} \text{km s}^{-1}$. In all panels, contours show the SMA+BGPS combined 1.3 mm continuum emission with identical levels as in the right panel of Figure 1. Dashed loops show the FWHM of the SMA primary beams. The synthesized beam of the SMA is shown in the lower left corner of each panel. In the SiO map, four candidates of shock heated regions are marked by boxes, which are also marked in Figures 6 & 7 and discussed in Section 4.3.2.

discuss its correlation with dust emission in Section 4.1.

3.2.2. Dense Gas Tracers

For the ^{13}CS line, the CSO data are contaminated by the atmospheric line, while the APEX data do not cover this frequency, so we use the SMA data only. For the other dense gas tracers, including H_2CO , HC_3N , and

CH_3CN , we use the combined SMA and CSO/APEX data. As shown in the integrated intensity maps in Figure 3, these lines all present compact emission at 0.1-pc scales, but the emission is not always spatially associated with the dense cores traced by compact dust emission. We will discuss spatial correlations between line emission and dust emission in detail in Section 4.1.

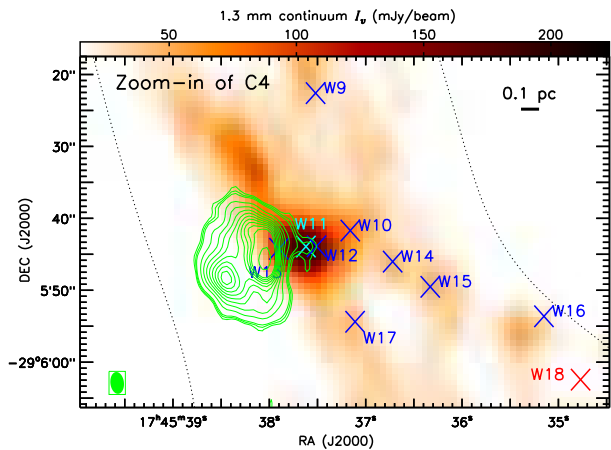


Figure 4. Green contours show the 1.3 cm continuum emission in the C4 clump. Levels are in steps of 2σ between 6σ and 10σ , steps of 10σ between 10σ and 100σ , and finally 150σ , in which $1\sigma=100 \mu\text{Jy beam}^{-1}$. The synthesized beam of the VLA observation is shown in the lower left corner. The SMA+BGPS 1.3 mm continuum emission is shown in the background, while H_2O masers detected by the VLA are marked by crosses. The maser W18 is consistent with a known AGB star and is marked by a red cross. The H_2O maser W11, which is spatially coincident with the compact 1.3 cm emission as well the C4-P1 dense core, is highlighted with cyan color. Properties of the other H_2O masers are reported in Lu et al. (2015).

3.2.3. Shock Tracers

The maps of SiO, HNC, SO, and CH_3OH in Figure 3 show the combined SMA and CSO/APEX data. All species present filamentary structures that have been seen in e.g. G0.253+0.016 as signatures of pc-scale shocks (Johnston et al. 2014). We will discuss the enhancement of these tracers in Section 4.2.

3.3. Embedded Ionizing Source in A Dense Core

As reported in Lu et al. (2015), the VLA 1.3 cm continuum observations confirm the existence of an H II region in the C4 clump (e.g., SgrA-G in Ho et al. 1985), with a peak intensity of 17.5 mJy/beam ($\sim 175\sigma$ levels). In addition, as shown in Figure 4, there is weak, compact 1.3 cm continuum emission on the western side of the H II region at $\sim 8\sigma$ levels. The image is not dynamic-range limited (Perley 1999), and the weak emission is unlikely due to side-lobes after a comparison with the dirty beam. This compact emission is spatially coincident with the C4-P1 dense core as well as the H_2O maser W11 (shown in Figure 4). It thus likely represents free-free emission from an embedded ultra-compact H II (UCH II) or hyper-compact H II (HCH II) region, which can be confirmed by follow-up radio recombination line observations. No other 1.3 cm continuum emission that can be associated with any dense cores is found in the cloud (see Figure 1 of Lu et al. 2015, for a complete 1.3 cm continuum map).

We fitted a 2D Gaussian to it and obtained a flux density of 1.5 mJy . The ionising photon rate, assuming optically thin continuum emission and an electron temperature of 10^4 K , is $1.1 \times 10^{46} \text{ s}^{-1}$ (Mezger et al. 1974), which can be produced by an early B-type star (no earlier than B0.5; Panagia 1973; Vacca et al. 1996). This is consistent with our estimate using H_2O maser luminosities in Lu et al. (2015), in which W11 was suggested to trace an early B-type protostar. In Section 4.3 we will discuss signatures of internal heating associated with this protostar.

3.4. VLA+GBT NH_3 Lines

The integrated intensities of the five inversion transitions of NH_3 represented by the zeroth moment are shown in Figure 5. For NH_3 (1, 1) and (2, 2), the integrated intensities include all hyperfine components between V_{lsr} of -30 and 50 km s^{-1} , because separating channels with only the main hyperfine lines is difficult due to broad linewidths and large velocity gradients across the cloud. For NH_3 (3, 3) to (5, 5), the integrated intensities only include the main hyperfine component between V_{lsr} of -20 and 40 km s^{-1} . The signal-to-noise ratio of the NH_3 (3, 3) line is much larger than the other four lines. To suppress noise, pixels below 10σ in the (3, 3) datacube were discarded when making the moments maps while for the other four lines pixels below 5σ were discarded.

The NH_3 emission, in particular that of NH_3 (3, 3), tends to be diffuse rather than concentrated on SMA dust peaks. Note that NH_3 (3, 3) belongs to the ortho species while the other four NH_3 lines belong to the para species (Ho & Townes 1983), between which transitions are very slow and can be ignored. Therefore, NH_3 (3, 3) can be treated as a different species from the other four lines, though the ortho/para ratio is usually in the range of 1–3 (e.g., Mills & Morris 2013).

The mosaic area of the VLA observations is larger than that of the SMA. In the extra area of the VLA maps that is not covered by the SMA observations, we found a likely filamentary feature on the western side of the cloud in all five transitions. This feature shows an apparently different centroid velocity (at -5 to 0 km s^{-1}) with the central part of the cloud. Its FWHM linewidths, measured with NH_3 (3, 3) lines, are between 6 and 8 km s^{-1} , similar to those in the 20 km s^{-1} cloud but larger than in the Galactic disk clouds ($\sim 1 \text{ km s}^{-1}$, Lu et al. 2014). In a more extended mapping obtained in the SMA Legacy Survey of the CMZ (CMZoom), multiple molecular line emission has been detected at the same location and velocity (C. Battersby, E. Keto, et al., in prep.). The feature may suggest an unassociated gas component in the foreground or background of the 20 km s^{-1} cloud, and is likely in the CMZ as well given

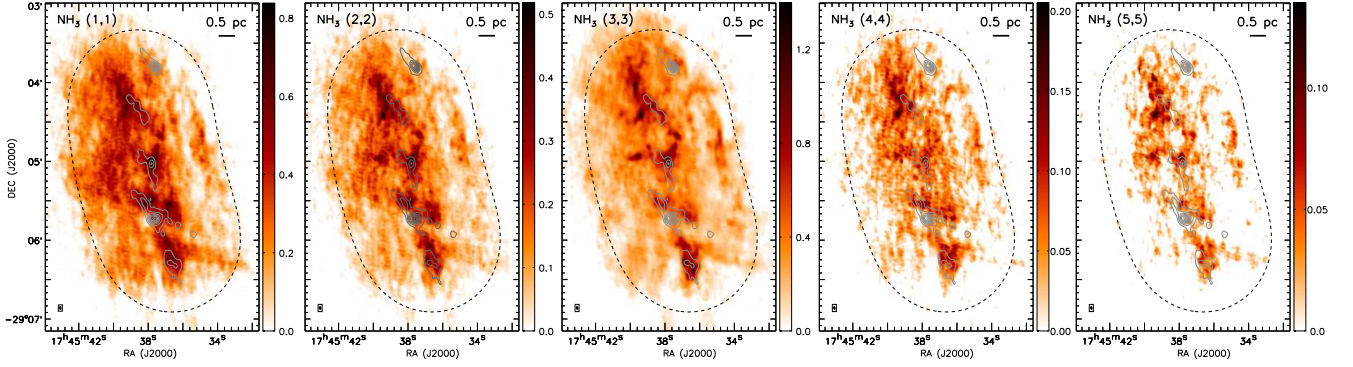


Figure 5. Integrated intensity maps (not corrected for primary beam responses) of the five NH_3 transitions from VLA+GBT combined data. The unit of the halftone scale is $\text{Jy beam}^{-1} \text{km s}^{-1}$. Contours show the SMA+BGPS 1.3 mm continuum emission with identical levels as in the right panel of [Figure 1](#). Dashed loops show the FWHM of the VLA primary beams. The synthesized beam of the VLA is shown in the lower left corner of each panel.

its large linewidth.

3.5. Kinetic Temperatures of Gas

We used the H_2CO transitions covered in the SMA+APEX observations and the NH_3 transitions covered in the VLA+GBT observations to estimate gas temperatures ([Ho & Townes 1983](#); [Walmsley & Ungerechts 1983](#); [Mangum & Wootten 1993](#)). Both transitions can be classified as para or ortho species due to orientations of spins of the multiple H nuclei and usually we only need to consider transitions between the same species.

First, we considered the H_2CO transitions. The three H_2CO transitions falling in the SMA+APEX band, $3_{0,3}-2_{0,2}$, $3_{2,2}-2_{2,1}$, and $3_{2,1}-2_{2,0}$, are all para species. The difference between upper level energies of the first transition and the latter two is ~ 47 K.

We have smoothed the H_2CO datacubes with a Gaussian kernel of $2''$ FWHM to increase signal-to-noise ratios, resulting in a larger beam size of $5''.5 \times 3''.4$. We based the following analysis of temperatures on the smoothed H_2CO data. In [Figure 6a](#) we show the peak intensity ratios between the $3_{2,1}-2_{2,0}$ and $3_{0,3}-2_{0,2}$ transitions for the whole cloud. Pixels where H_2CO $3_{2,1}-2_{2,0}$ or $3_{0,3}-2_{0,2}$ signals are below 5σ levels were masked. Since the $3_{2,1}-2_{2,0}$ transition has a higher upper level energy, larger ratios between the two transitions qualitatively represent higher gas temperatures.

We employed the RADEX code ([van der Tak et al. 2007](#)) with a modified solver `myRadex`¹⁷ to implement the non-local-thermodynamic-equilibrium (non-LTE) conditions. The collision rates between H_2CO and ortho/para- H_2 were taken from LAMDA ([Wiesenfeld & Faure 2013](#)). The ortho/para ratios of H_2 were calculated based on kinetic temperatures. We as-

sumed a uniform spherical geometry, and fixed the velocity gradient to a representative value of $5 \text{ km s}^{-1} \text{pc}^{-1}$, then generated H_2CO intensities expected from models when kinetic temperatures range between $10^{0.5}$ K and 10^3 K in logarithmic steps of 0.1, H_2 number densities between 10^2 and 10^8 cm^{-3} in logarithmic steps of 0.1, and column densities between $10^{22.3}$ and $10^{23.8} \text{ cm}^{-2}$ in logarithmic steps of 0.1. The abundance of H_2CO to H_2 is assumed to be 10^{-9} ([Ao et al. 2013](#)), hence the H_2CO column densities we were using in the models are between $10^{13.3}$ and $10^{14.8} \text{ cm}^{-2}$. We have assumed a single velocity component and a beam filling factor of 1 throughout the analysis.

We used a customized routine ([Zhang et al. 2014](#)) to determine the most likely gas temperatures as well as H_2 densities that can reproduce the observed H_2CO $3_{0,3}-2_{0,2}$ intensities as well as the observed H_2CO $3_{2,2}-2_{2,1}$ to $3_{0,3}-2_{0,2}$ line ratios. An example is shown in [Appendix A](#) while details of this procedure can be found in [Zhang et al. \(2014\)](#).

One feature we noticed is that the H_2CO $3_{2,2}-2_{2,1}$ to $3_{0,3}-2_{0,2}$ line ratios, $R(3_{2,2}-2_{2,1}/3_{0,3}-2_{0,2})$, are sensitive to kinetic temperatures, but not so to H_2 densities or column densities. In light of this, in [Appendix A](#) we fitted the line ratios versus the kinetic temperatures and derived an analytical expression:

$$T_{\text{kin}} = 17.5 \exp(4.27 R(3_{2,2}-2_{2,1}/3_{0,3}-2_{0,2})) \text{ K}. \quad (1)$$

This equation could reproduce the kinetic temperatures from RADEX modelling as accurate as 0.08 dex (20%) between $T_{\text{kin}} = 30-300$ K. The temperatures derived from RADEX modelling have uncertainties of 0.15 dex (40%) themselves, as discussed in [Appendix A](#), which include both systematic errors with assumed density, column density, and abundance, as well as random errors with the observed H_2CO intensities. The overall uncertainty in the temperatures derived from [Equation 1](#) would be 0.17 dex ($\sim 50\%$). We applied this relation to

¹⁷ <https://github.com/fjdu/myRadex>

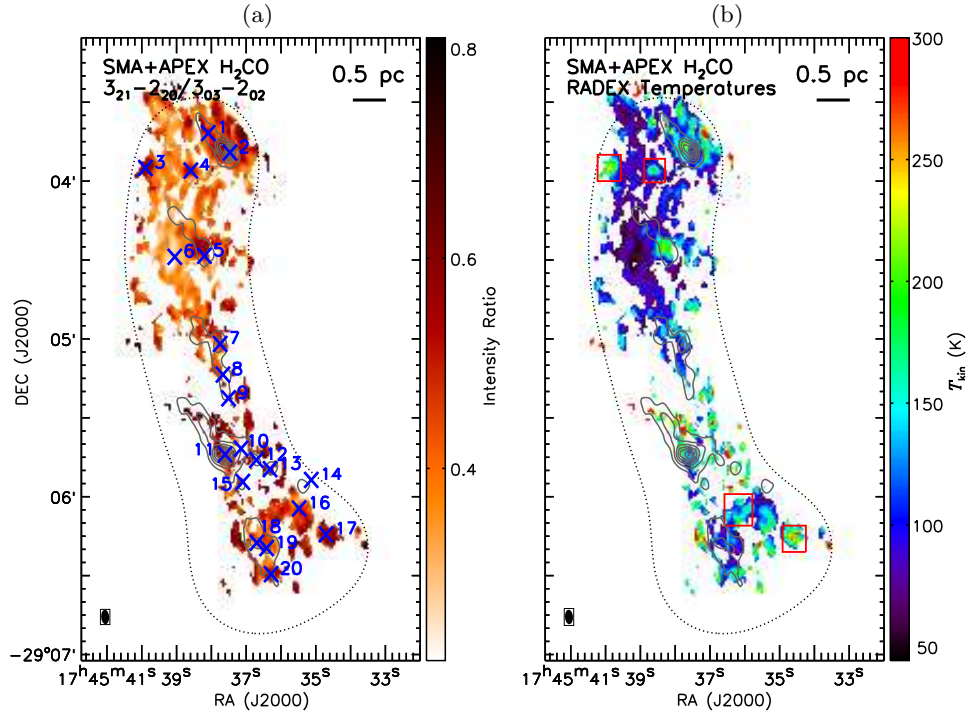


Figure 6. Contours in both panels represent SMA+BGPS 1.3 mm continuum emission with identical levels as in the right panel of Figure 1. Dashed loops show the FWHM of the SMA primary beams. The enlarged beam after smoothing, $5''.5 \times 3''.4$, is shown in the lower left corner of each panel. (a) Ratios of peak intensities of SMA+APEX H_2CO lines. The cyan crosses mark the positions where we extracted the temperatures and linewidths in Table 2 and Figure 10. (b) Kinetic temperatures derived with RADEX modelling in Section 3.5. Four candidates of shock heated regions are marked by boxes (cf. the SiO map in Figure 3).

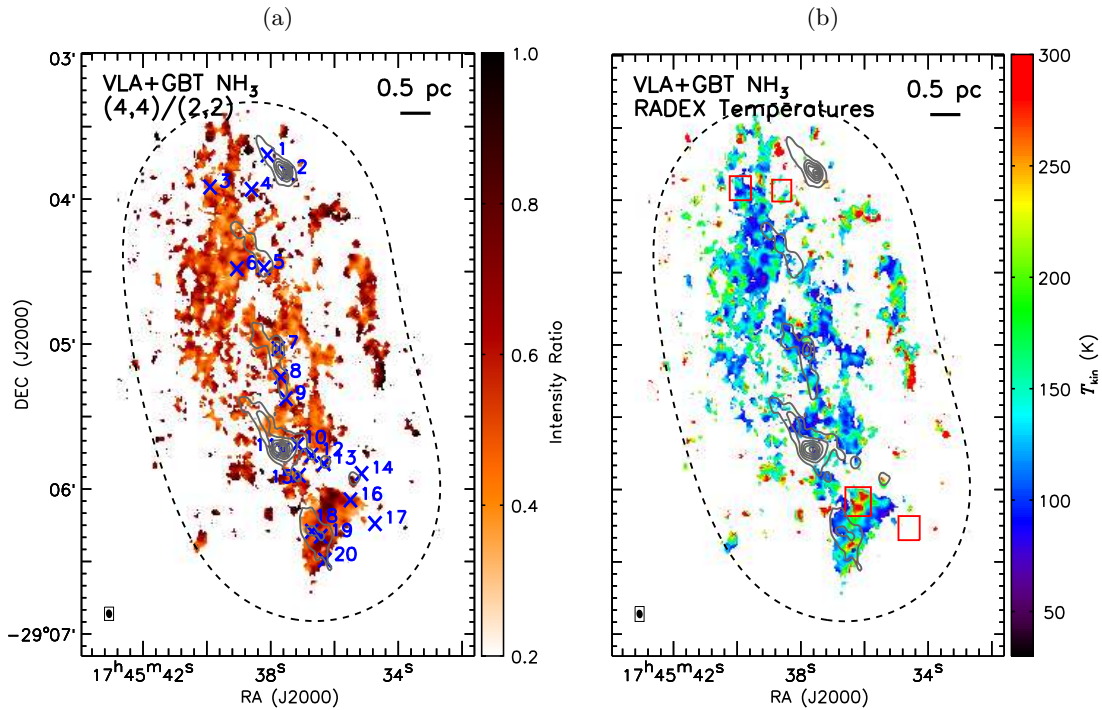


Figure 7. Contours in both panels represent SMA+BGPS 1.3 mm continuum emission with identical levels as in the right panel of Figure 1. Dashed loops show the FWHM of the VLA primary beams. The enlarged beam after smoothing, $3''.6 \times 2''.9$, is shown in the lower left corner of each panel. (a) Ratios of peak intensities of VLA+GBT NH_3 lines. The cyan crosses are the same as in Figure 6. (b) Kinetic temperatures derived with RADEX modelling in Section 3.5. Four candidates of shock heated regions are also marked by boxes as in Figure 6. the line ratio map in Figure 6a and derived a kinetic temperature map as shown in Figure 6b.

Second, we considered the VLA NH_3 transitions. Among the five transitions, the NH_3 (1, 1), (2, 2), (4, 4), and (5, 5) are all para species thus can be jointly considered. Unfortunately, the NH_3 (1, 1) lines suffer from strong absorption, while the NH_3 (5, 5) lines are usually weak, therefore we chose the (2, 2) and (4, 4) lines to estimate temperatures. The difference between their upper level energies is ~ 137 K.

We smoothed the NH_3 datacubes with a Gaussian kernel of $2''$ FWHM to increase signal-to-noise ratios, resulting in a beam size of $3''.6 \times 2''.9$. We masked pixels where NH_3 (2, 2) or (4, 4) signals are below 5σ and showed the peak intensity ratios between main components of these two transitions for the whole cloud in Figure 7a. In addition, similar to the above analysis with the H_2CO lines, we derived kinetic temperatures under non-LTE conditions with the VLA+GBT NH_3 (2, 2) and (4, 4) transitions. The collision rates between NH_3 and para- H_2 were taken from LAMDA (Danby et al. 1988). The ortho/para ratios of H_2 were calculated based on kinetic temperatures. We assumed a NH_3 to H_2 abundance of 3×10^{-8} (Harju et al. 1993), and used identical model grids as for H_2CO . An example is shown in Appendix A. We also derived a relation between NH_3 (4, 4) to (2, 2) line ratios, $R(44/22)$ and kinetic temperatures:

$$T_{\text{kin}} = 31.2 \exp(2.75 R(44/22)) \text{ K}, \quad (2)$$

which could reproduce temperatures from RADEX modelling as accurate as 0.08 dex ($\lesssim 20\%$) between $T_{\text{kin}} = 30\text{--}300$ K. We assumed an overall uncertainty of 0.18 dex ($\sim 50\%$) in the temperatures after adding in the uncertainties in the RADEX modelling as discussed in Appendix A. The kinetic temperatures derived using the observed line ratios with this equation are shown in Figure 7b. More discussions on the gas temperatures can be found in Section 4.3.

4. DISCUSSION

4.1. Correlation between the Dust and Spectral Line Emission

We study the spatial correlation between dust emission and spectral lines in order to understand the effect of star formation on the molecular gas environment. As demonstrated in Section 3.1, the compact dust emission traces gravitationally bound dense cores at 0.1-pc scales in which we found a population of H_2O masers. Therefore, it is a reasonable indicator of star formation in the 20 km s^{-1} cloud. Correlations between the compact dust emission from dense cores and spectral lines will help to reveal underlying connections of such lines to star formation.

Here we attempt to quantitatively characterize which lines are spatially correlated with the compact dust

Table 1. 2D cross-correlation coefficients between the dust and the molecular lines.

Transitions	Coefficients with SMA-only dust	Coefficients with SMA+BGPS dust
^{13}CO 2-1	0.36	0.78
C^{18}O 2-1	0.40	0.80
H_2CO 3 _{0,3} -2 _{0,2}	0.37	0.78
H_2CO 3 _{2,2} -2 _{2,1}	0.41	0.58
H_2CO 3 _{2,1} -2 _{2,0}	0.43	0.61
CH_3CN 12-11, K=0,1	0.43	0.30
HC_3N 24-23	0.19	0.19
^{13}CS 5-4	0.35	0.23
HNCO 10 _{0,10} -9 _{0,9}	0.48	0.79
SO 6 ₅ -5 ₄	0.54	0.74
CH_3OH 4 _{2,2} -3 _{1,2}	0.56	0.79
CH_3OH 8 _{-1,8} -7 _{0,7}	0.60	0.60
SiO 5-4	0.40	0.64
NH_3 (1, 1)	0.41	0.81
NH_3 (2, 2)	0.39	0.78
NH_3 (3, 3)	0.40	0.80
NH_3 (4, 4)	0.32	0.69
NH_3 (5, 5)	0.27	0.58

emission based on the 2D cross-correlation analysis¹⁸.

We take the SMA-only dust emission image and the SMA+BGPS combined dust emission image (the middle and right panels of Figure 1), to represent the compact emission from the dense cores and the diffuse dust emission, respectively. The SMA+BGPS dust emission image is used as a control sample. We reset pixels with negative intensities in these two images to 0 to keep only emission.

In addition to the SMA+CSO/APEX data, we take the VLA+GBT NH_3 integrated intensities maps and convolve them with the SMA primary beams. We are aware that sensitivities and dynamic ranges of the SMA and VLA observations are different, which may make a direct comparison between the 1.3 mm lines and the NH_3 lines problematic. Nevertheless, we include the NH_3 lines here for reference.

Then we normalize all the images with respect to their maximum intensities. The images under consideration are, or have been regridded, in the same coordinates, so we only need to calculate their cross-correlation coefficients, without spatially shifting one image relative to the other in order to find the maximum cross-correlation. The 2D cross-correlation coefficients de-

¹⁸ Based on the IDL function ‘correl_images.pro’: https://idlastro.gsfc.nasa.gov/ftp/pro/image/correl_images.pro.

rived in such way will be between -1 and 1 , with -1 being anti-correlated, 0 being not correlated at all, and 1 being correlated.

The 2D cross-correlation coefficients between the dust emission images and the spectral line integrated intensity maps are listed in [Table 1](#). First, we consider correlations with the compact dust emission represented by the SMA-only dust image. Among the 18 spectral lines, the two CH_3OH lines and the SO line have 2D cross-correlation coefficients with the compact dust emission of >0.50 . The HNCO line also has a coefficient of 0.48 . On the other hand, the three H_2CO lines and the five NH_3 lines, which are conventional dense gas tracers for Galactic disk clouds, have smaller coefficients of 0.37 – 0.43 and 0.27 – 0.41 , respectively. Second, we consider correlations with the control sample, the diffuse dust emission represented by the SMA+BGPS dust emission image. Large 2D cross-correlation coefficients of ~ 0.8 are found for ^{13}CO , C^{18}O , HNCO , one H_2CO line, one CH_3OH line, and three NH_3 lines. As seen in [Figures 3 & 5](#), these lines do present diffuse emission. The CH_3CN , ^{13}CS , HC_3N , and $\text{CH}_3\text{OH } 8_{-1,8}-7_{0,7}$ lines have the same or smaller 2D cross-correlation coefficients with the diffuse dust emission than with the compact dust emission. This happens when the line emission is concentrated on the compact dust emission.

Based on the 2D cross-correlation analysis, the SO line, the HNCO line, and the two CH_3OH lines are best correlated spatially with the compact dust emission from dense cores among all the detected lines. We also examine the correlations with a visual inspection of the maps in [Figure 3](#). Indeed, several emission peaks of these lines spatially coincident with the dense cores we identified, although emission peaks that are not associated with any dust emission are also found (e.g., in the south-western part of the cloud). The most notable line is $\text{CH}_3\text{OH } 8_{-1,8}-7_{0,7}$, which presents emission peaks toward all five massive clumps and is concentrated on dust cores. These lines have been observed to be enhanced by shocks ([Bachiller & Pérez Gutiérrez 1997](#); [Rodríguez-Fernández et al. 2010](#)), but our result suggests that they also trace the dense cores in the 20 km s^{-1} cloud well. A potential explanation is that they are enhanced by star formation embedded in the dense cores, as discussed in [Section 4.2](#).

The three H_2CO and the five NH_3 lines appear to be correlated with the compact dust emission in the dense cores, but with smaller 2D cross-correlation coefficients than the four lines above. As shown in [Figures 3 & 5](#), the two species do not present strong emission in the brightest dust peaks in the C4 clump, and NH_3 emission is also absent in the C1 clump. At 0.1 -pc scales in this cloud, they are not good tracers of dense gas. The reason could be strong shocks in the cloud that destroy

molecules.

At last, although the CH_3CN , HC_3N and ^{13}CS lines have small 2D cross-correlation coefficients, a visual inspection of [Figure 3](#) suggests that their emission is detected preferably on the dense cores. They are fainter than the lines discussed above, hence in our sensitivity-limited observations they present a large fraction of area of non-detection thus tend to have small 2D cross-correlation coefficients with the dust emission images. In particular, CH_3CN is usually detected in hot molecular cores (e.g., [Araya et al. 2005](#)), and has hyperfine splittings that are suitable to determine gas temperatures of $>100 \text{ K}$. Therefore, sensitive spectral line observations that are able to detect faint CH_3CN emission will be useful for studying embedded high-mass star formation in these dense cores.

Overall, the 2D cross-correlation coefficients between the dust and spectral line emission we found are larger than the results of [Rathborne et al. \(2015\)](#), which discussed the dust emission and various spectral lines at 3 mm in G0.253+0.016 . We stress that a direct comparison between different observations is inappropriate. [Rathborne et al. \(2015\)](#) argued that the low 2D cross-correlation coefficients are due to the optically thick molecular line emission. The dust emission traced by 3 mm continuum also shows a lack of compact substructures. These factors may lead to the smaller cross-correlation coefficients between the dust and molecular line emission in G0.253+0.016 .

4.2. The Enhancement in Emission of Shock Tracers towards Massive Clumps

We use the enhancement of line ratios between shock tracers to reveal the relative shock strength in the cloud. The SMA+CSO/APEX observations detected several shock tracers, including SiO , CH_3OH , HNCO , and SO . It has been suggested that relatively fast shocks ($\gtrsim 20 \text{ km s}^{-1}$) can destroy dust grains and release silicon (Si) into the gas phase ([Guillet et al. 2009](#))¹⁹, while relatively slow shocks ($\lesssim 20 \text{ km s}^{-1}$) can evaporate ice mantles and release molecules such as CH_3OH , HNCO , and SO ([Garay et al. 2000](#); [Rodríguez-Fernández et al. 2010](#)) which in turn could be destroyed by fast shocks ([Garay et al. 2000](#); [Kelly et al. 2017](#)). Therefore, the SiO and $\text{CH}_3\text{OH}/\text{HNCO}/\text{SO}$ lines can be used as tracers of fast and slow shocks, respectively, and line ratios between them are related to shock strength (e.g., [Usero et al. 2006](#); [Kelly et al. 2017](#)). However it must be noted that ice mantle evaporation in hot molecular cores

¹⁹ Widespread detection of SiO throughout the CMZ ([Jones et al. 2012](#)) raises questions about this interpretation. Similarly, [Jiménez-Serra et al. \(2010\)](#) detected diffuse SiO emission in a region with only low-velocity shocks.

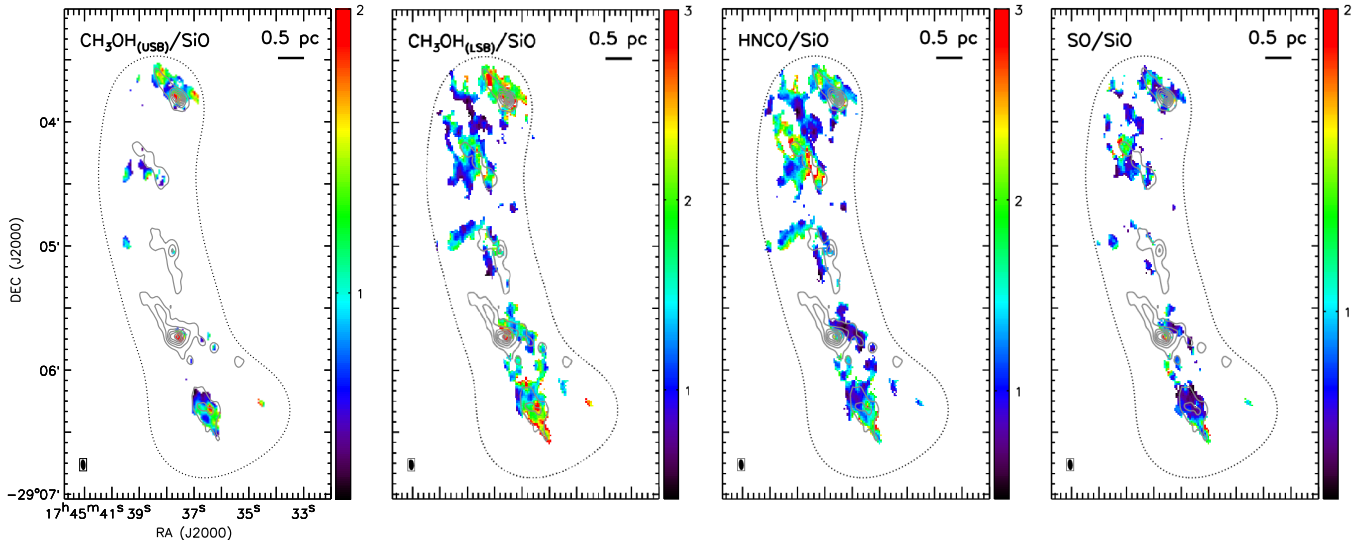


Figure 8. Each of the four panels shows integrated intensity ratios between one of the ‘slow shock tracers’ (CH_3OH 8_{-1,8}-7_{0,7} labeled as ‘USB’ & 4_{2,2}-3_{1,2} labeled as ‘LSB’, HNC0 10_{0,10}-9_{0,9}, and SO 6₅-5₄) and SiO 5-4. Contours in all panels represent SMA+BGPS 1.3 mm continuum emission with identical levels as in the right panel of Figure 1. The CH_3OH 8_{-1,8}-7_{0,7}/ SiO and SO/SiO ratio larger than 2, and the CH_3OH 4_{2,2}-3_{1,2}/ SiO and $\text{HNC0}/\text{SiO}$ ratios larger than 3 are truncated in the maps, which correspond to about twice of the mean ratios, to better illustrate the enhancement of line ratios.

can also be responsible for the enhancement of CH_3OH , HNC0 , or SO emission (Garrod & Herbst 2006).

In Figure 8, we present the ratios of integrated intensities between $\text{CH}_3\text{OH}/\text{HNC0}/\text{SO}$ and SiO . To suppress the low signal-to-noise emission, we have excluded pixels with integrated intensities $< 3.6 \text{ Jy beam}^{-1} \text{ km s}^{-1}$ ($\sim 5\sigma$) for all the lines when making the ratios.

The line ratios between $\text{CH}_3\text{OH}/\text{HNC0}/\text{SO}$ and SiO show clear enhancement toward the compact dust emission as shown in Figure 8. Based on the spatial distribution of the shock tracers, we speculate that fast shocks of $\gtrsim 20 \text{ km s}^{-1}$ traced by the widespread SiO emission are processing gas in the entire cloud. Meanwhile, the increased line ratios of the ‘slow shock tracers’ toward the compact dust emission suggest two possible scenarios²⁰. First, slow shocks of $\lesssim 20 \text{ km s}^{-1}$ in these regions can release these molecules. The origin of slow shocks is to be determined. Second, hot molecular cores may evaporate these molecules from dust. In particular, the C1 and C4 clumps are associated with luminous H_2O masers, and C4 is also associated with an UCH II region, hence they likely harbor high-mass protostars. In such scenario, the enhanced CH_3OH , HNC0 , and SO emission in these clumps are due to star formation. Future sensitive spectral line observations with e.g. the Atacama Large Millimeter/submillimeter Array (ALMA) of CH_3CN lines in these regions will help to tell the

²⁰ A third possibility is that photodissociation, X-ray, or cosmic ray destroy $\text{CH}_3\text{OH}/\text{HNC0}/\text{SO}$ molecules in diffuse gas but cannot affect those in dense cores. However the widespread emission of these lines in the cloud makes it unlikely.

existence of hot molecular cores hence verify the two scenarios.

4.3. Gas Temperatures at 0.1-pc Scales

As shown in Section 3.5, the gas temperatures derived from H_2CO and NH_3 lines are higher than the dust temperatures in the 20 km s^{-1} cloud that are at ~ 18 -30 K (Molinari et al. 2011). Such discrepancy between gas and dust temperatures has been observed in the CMZ at $\gtrsim 1 \text{ pc}$ spatial scales (e.g., Ao et al. 2013; Mills & Morris 2013; Ott et al. 2014; Ginsburg et al. 2016; Immer et al. 2016; Krieger et al. 2016). Our observations confirm that in the 20 km s^{-1} cloud high gas temperatures of $\gtrsim 50 \text{ K}$ continue down to 0.1-pc scales. However, no observations of dust temperatures in this cloud at 0.1-pc scales have been made, making a direct comparison between gas and dust temperatures infeasible.

4.3.1. Gas Temperatures Derived from Different Tracers

We compare gas temperatures derived from the H_2CO and NH_3 lines. We first regrid the NH_3 (2, 2) and (4, 4) datacubes to the H_2CO maps that have larger pixel size, then derive temperatures based on NH_3 line ratios following the procedures in Section 3.5. The offset between the resulting temperature map and the original NH_3 temperature map in Figure 7 is $\lesssim 5 \text{ K}$ for most of the pixels, but increases to 30 K on boundaries of emission where signal-to-noise ratios are lower. Pixels with large temperature offsets are a small fraction of the map, and the offset is comparable to the uncertainty of the temperatures, therefore we consider the regridded temperature map to be acceptable.

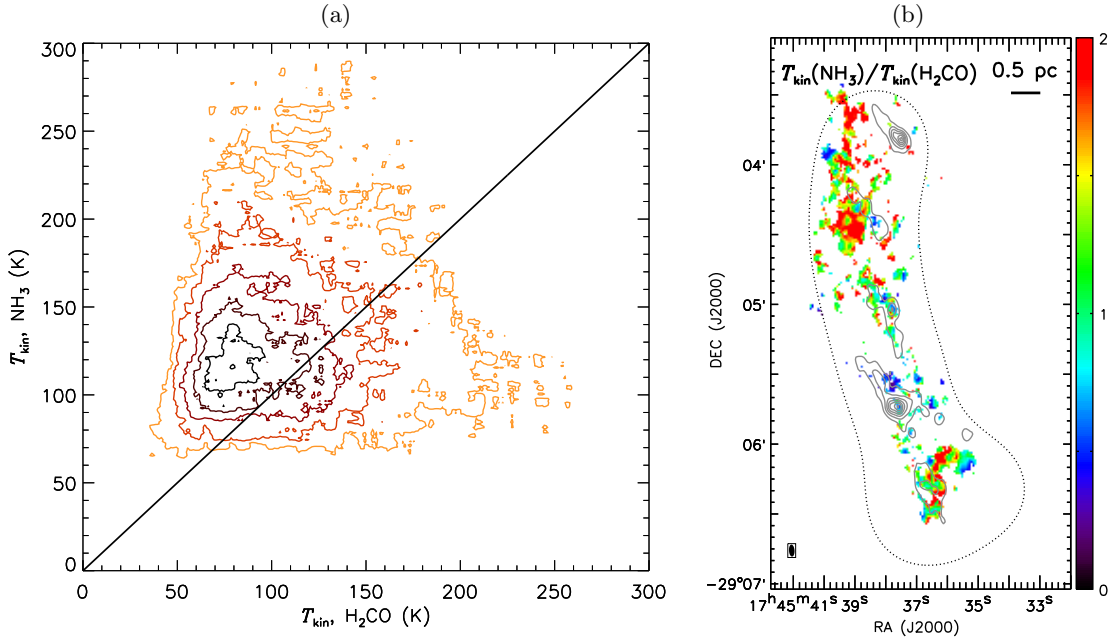


Figure 9. Comparison between temperatures derived from NH_3 and H_2CO lines. (a) Density plot of kinetic temperatures derived from H_2CO and NH_3 lines for pixels where both temperatures are available. Contour levels are between 10% and 90%, from lightest to darkest colors, in step of 20%, meaning the percentage of data points outside of the given level. The diagonal line shows where the two temperatures are equal. (b) Ratio map of kinetic temperatures derived from NH_3 and H_2CO . Ratios above 2 (up to a maximum of 4.7) are truncated to 2. Only pixels where both temperatures are available are displayed. Contours show SMA+BGPS 1.3 mm continuum emission with identical levels as in the right panel of Figure 1.

The regridded NH_3 temperature map is compared with the temperature map derived from H_2CO lines (Figure 6b). As shown in Figure 9a, for pixels where both H_2CO and NH_3 temperatures are available, temperatures derived from the two tracers are poorly correlated. This poor correlation is likely due to the large uncertainties in both temperatures.

One feature in Figure 9a is a slight overpopulation in higher temperatures with NH_3 than with H_2CO . This can be also seen in the temperature ratio map in Figure 9b. In the northeastern side of the cloud, temperatures with NH_3 are ~ 200 K, while temperatures with H_2CO are $\lesssim 100$ K, resulting in ratios of $\gtrsim 2$. Similar high ratios are found in the southwestern side of the cloud, where temperatures with NH_3 are > 200 K and those with H_2CO are ~ 150 K. Such large temperature ratios are unlikely due to the 50% uncertainties in temperatures. Given that the H_2CO lines have higher critical densities than the NH_3 lines ($\sim 10^5 \text{ cm}^{-3}$ vs. $\sim 10^{3-4} \text{ cm}^{-3}$), the two molecules may trace two gas components in these high-temperature-ratio regions: a less dense and warmer component traced by NH_3 lines, and a denser and colder component traced by H_2CO lines.

On the other hand, temperature ratios of < 1 are also found. One example is the dense core C4-P1, whose temperature derived from H_2CO lines is higher than from NH_3 lines (~ 120 K vs. ~ 70 K, Appendix A; also see

position 11 in Table 2) despite large uncertainties. The density derived from H_2CO is also larger than from NH_3 , although the densities highly depend on the assumed column densities and abundances. This may suggest internal heating in C4-P1, if this dense core has a centrally peaked density profile. The heating source could be embedded high-mass protostars, traced by H_2O masers and UCH II regions (see Section 3.3). Other candidates of such internally heated dense cores include C1-P1, C2-P1, C4-P4, and C4-P5 (positions 2, 5, 12, and 13, respectively in Table 2).

In addition, the gas temperatures with H_2CO at 0.1-pc scales are systematically higher than those at 1-pc scales. Ao et al. (2013), Ginsburg et al. (2016), and Immer et al. (2016) derived temperatures of 50–100 K in the 20 km s^{-1} cloud with single-dish H_2CO data. In Figure 6c, high temperatures of > 200 K are found at 0.1-pc scales, especially toward the C1, C2, and C5 clumps. If we smooth our SMA+APEX H_2CO data to the angular resolution of $30''$ to match with the single-dish observations, the $\text{H}_2\text{CO } 3_{2,2}-2_{2,1}$ to $3_{0,3}-2_{0,2}$ line ratios range from 0.27 to 0.45 and the temperatures from RADEX modelling are 50–120 K. Therefore, the discrepancy is likely due to the angular resolution, and our observations suggest that high-temperature spots of > 200 K exist at 0.1-pc scales.

4.3.2. Turbulent Heating and Protostellar Heating

Table 2. Temperatures, linewidths, and H_2O maser luminosities of selected positions.

Position ID	R.A. & Decl. (J2000)	T_{kin} , H_2CO (K)	FWHM, H_2CO (km s^{-1})	T_{kin} , NH_3 (K)	FWHM, NH_3 (km s^{-1})	$L_{\text{H}_2\text{O}}$ ($10^{-7} L_{\odot}$)	Associated H_2O masers
1	17:45:38.10, -29:03:41.75	250	15.7 ± 1.0	177	10.7 ± 1.9	7.0	W1
2	17:45:37.48, -29:03:49.15	105	8.5 ± 1.3	87	9.5 ± 1.1	61.8	W3
3	17:45:39.90, -29:03:55.00	215	14.6 ± 1.2	114	15.7 ± 0.8
4	17:45:38.60, -29:03:56.00	162	16.6 ± 1.3	153	13.7 ± 1.1
5	17:45:38.21, -29:04:28.40	151	14.9 ± 0.8	138	19.4 ± 1.3
6	17:45:39.06, -29:04:28.80	64	7.7 ± 0.3	138	10.0 ± 0.7
7	17:45:37.76, -29:05:01.91	117	7.6 ± 0.5	159	6.2 ± 0.7	110.0	W5
8	17:45:37.68, -29:05:13.57	105	11.8 ± 1.0	127	5.4 ± 0.6	0.3	W8
9	17:45:37.52, -29:05:22.59	124	10.4 ± 1.4	141	4.1 ± 0.6	0.7	W9
10	17:45:37.16, -29:05:41.70	169	9.6 ± 0.8	232	8.8 ± 0.9	3.2	W10
11	17:45:37.62, -29:05:43.92	134	5.8 ± 0.8	76	8.1 ± 1.0	53.0	W11
12	17:45:36.72, -29:05:46.02	135	13.1 ± 1.3	77	7.5 ± 2.3	4.0	W14
13	17:45:36.33, -29:05:49.52	257	15.8 ± 1.1	126	6.1 ± 0.8	38.7	W15
14	17:45:35.15, -29:05:53.62	78	15.6 ± 0.9	104	8.0 ± 1.5	0.8	W16
15	17:45:37.11, -29:05:54.38	127	6.8 ± 0.6	249	8.9 ± 0.6	4.9	W17
16	17:45:35.50, -29:06:04.50	132	13.5 ± 0.5	107	7.0 ± 0.6
17	17:45:34.73, -29:06:14.30	208	11.0 ± 2.0	103	4.7 ± 0.3
18	17:45:36.71, -29:06:17.50	102	13.3 ± 1.1	109	6.7 ± 0.4
19	17:45:36.43, -29:06:19.55	108	8.4 ± 0.9	166	5.1 ± 0.3
20	17:45:36.30, -29:06:29.43	157	21.4 ± 1.2	192	9.2 ± 0.7

We make use of the temperature maps derived from H_2CO and NH_3 lines to understand heating mechanisms in the cloud. As discussed in [Ao et al. \(2013\)](#), [Ginsburg et al. \(2016\)](#), and [Immer et al. \(2016\)](#), turbulent heating can reproduce the observed gas temperatures at >1 -pc scales in the CMZ. When it comes to 0.1-pc scales, turbulent heating can be still present. As discussed in [Ginsburg et al. \(2016\)](#), the temperature can be well mixed on milliparsec scales in kiloyear timescales for turbulent heating. Indirect evidence of turbulent heating in the northern end of the 20 km s^{-1} cloud has been suggested with arguments from enhanced NH_3 emission and $\text{SiO}/\text{C}^{34}\text{S}$ line ratios ([Wright et al. 2001](#); [Liu et al. 2013](#)).

In addition, in the 20 km s^{-1} cloud where we have found signatures of star formation, we need to take protostellar heating into account. Gas temperatures of >100 K have been observed at <0.1 pc spatial scales towards hot molecular cores ([Araya et al. 2005](#)). If the luminous H_2O masers we detected indeed trace high-mass star formation, then it is possible to observe temperatures of >100 K at 0.1-pc scales once the protostars evolve to a phase of hot molecular cores. If such protostars exist, they should warm up the dust and produce significant mid-infrared emission, which is in contrast with the non-detection of point sources other than the

known H II region at mid-infrared wavelengths in the 20 km s^{-1} cloud ([Yusef-Zadeh et al. 2009](#)). The reason could be strong extinction: with a characteristic hydrogen column density of $4 \times 10^{23} \text{ cm}^{-2}$ in the 20 km s^{-1} cloud (C. Battersby et al. in prep.), the extinction at mid-infrared ($\sim 5\text{--}30 \mu\text{m}$) is $\sim 10\text{--}20$ mag ([Draine 2003](#)). High-mass star-forming regions with typical bolometric luminosities of $\sim 10^5 L_{\odot}$ ([Sridharan et al. 2002](#)) have an absolute bolometric magnitude of -7.8 , and an apparent magnitude of ~ 6.8 at the distance of the CMZ. Adding the extinction will bring their apparent magnitude down to 16.8–26.8, hence make them below the detection limit at mid-infrared in [Yusef-Zadeh et al. \(2009\)](#).

We take two approaches to explore the effect of turbulent and protostellar heating. First, we search for correlations between temperatures and linewidths, assuming the latter to be an indicator of turbulent strength (cf. [Ginsburg et al. 2016](#); [Immer et al. 2016](#)), and between temperatures and H_2O maser luminosities, assuming the latter to be correlated with protostellar luminosities ([Palla et al. 1993](#)). Second, we attempt to look for direct signatures of turbulent or protostellar heating from our temperature maps. Evidence of strong turbulence is based on SiO emission, while evidence of star formation comes from masers and UCH II regions in dense cores.

In the first approach, we select 20 representative po-

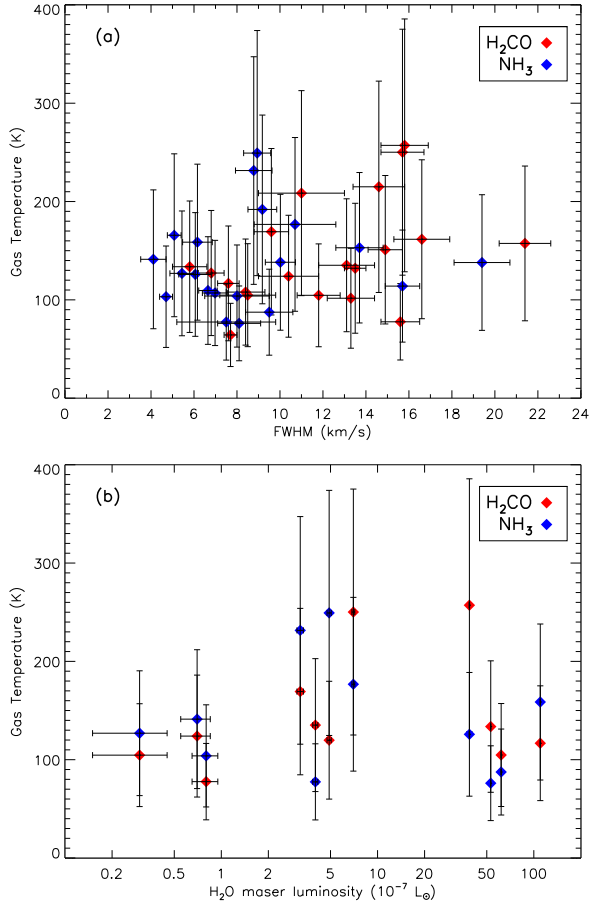


Figure 10. (a) The mean temperatures and FWHM linewidths from 18 representative positions in Figures 6a & 7a. The errors in the temperatures are assumed to be 50%, while the errors in the linewidths are taken from Table 2. (b) The mean temperatures and H₂O maser luminosities from 11 positions in Figure 6. The errors in the temperatures are the same as in panel (a) and the errors in luminosities are based on the rms of 6 mJy per 0.2 km s⁻¹ of the VLA H₂O maser observations (Lu et al. 2015).

sitions in Figures 6 & 7, and derive their temperatures from the mean H₂CO or NH₃ spectra within a 5''-diameter circle (~ 0.2 pc at the distance of the CMZ). The size of 0.2 pc is chosen because protostellar heating usually affect local gas in a radius of $\lesssim 0.1$ pc (Longmore et al. 2011) out of which the temperatures drop to < 50 K. These positions locate both on dense cores and offset from any dense cores.

The results are listed in Table 2. In Figure 10a, we plot the temperatures versus the linewidths. The temperatures are derived directly from the observed line ratios using Equations 1 & 2 to simplify the process. The linewidths are measured with the mean H₂CO 3_{2,1}-2_{2,0} or NH₃ (4, 4) spectra by fitting a Gaussian profile, with 1- σ errors from the fittings listed in Table 2. For spectra with obvious multiple velocity components, we try to fit two Gaussian profiles simultaneously and take the

stronger one.

We derive the Pearson correlation coefficients between the temperatures and the linewidths, using inverse squares of the uncertainties in temperatures (50%) as weighting factors. We do not include the uncertainties of linewidths in the weighting factors because they are less significant. The weighted correlation coefficients, with H₂CO data only, NH₃ data only, and all data together, are 0.32, 0.13, and 0.22, respectively. They suggest weak to no correlations between the temperatures and the linewidths. This is in contrast to the statistically significant correlation found at 1-pc scales in several other CMZ clouds in Immer et al. (2016).

In Figure 10b, we plot the temperatures versus the luminosities of the associated H₂O masers, if there are any, in Figure 10b. A H₂O maser must be within 3'' projected of the selected position (~ 0.1 pc projected distance) to be considered as associated. At last, we find 11 positions with associated H₂O masers. The weighted Pearson correlation coefficient with all data together is 0.08. Therefore, no correlation is found between the temperatures and maser luminosities.

The temperature-linewidth and temperature-maser luminosity data suffers from several uncertainties. Although we have excluded most of the systematic motions in the cloud by resolving the dense cores at 0.1-pc scales, the linewidth may still be contaminated by unresolved multiple velocity components thus may not be a good indicator of turbulence. Likewise, using H₂O masers as a star formation tracer has large uncertainties (e.g., the occurrence rate and variability of H₂O masers). Therefore, such non-correlations are not straightforward for understanding heating of gas.

In the second approach, we directly search for turbulent or protostellar heated regions in the high-angular-resolution maps from the SMA and VLA observations. This avoids the ambiguities, e.g., using linewidths to trace turbulence, hence is more straightforward.

We notice four candidates of shock heated regions that are marked by boxes in Figures 3, 6, & 7. On the one hand, in the SiO map in Figure 3, these regions show SiO emission that usually traces fast shocks, but are offset from compact dust emission hence are unlikely associated with protostars. On the other hand, as shown in Figures 6 & 7, temperatures in these regions ($\gtrsim 200$ K) tend to be higher than their environment. Therefore, these regions are likely heated by shocks.

We also find a candidate of internally heated dense cores, C4-P1, as discussed in Section 4.3.1. Combining with evidence of high-mass star formation in this dense core (Section 3.3), it is likely internally heated by embedded high-mass protostars. Several dense cores, such as C1-P1, C2-P1, C4-P4, and C4-P5 also show higher temperatures with H₂CO than with NH₃ thus are likely

internally heated, although their protostellar nature is to be confirmed. Future sensitive spectral line (e.g., multiple CH_3CN) observations with ALMA in these candidates will help to derive their temperature profiles and confirm the embedded heating sources.

Therefore, with the second approach we find evidence of both turbulent and protostellar heating at 0.1-pc scales in the 20 km s^{-1} cloud. Turbulent heating seems to be widespread in the cloud, while protostellar heating is localized in dense cores around protostars.

5. CONCLUSIONS

We have used the SMA 1.3 mm spectral line observations, the VLA NH_3 line observations, as well as complementary single-dish observations to study properties of dense gas in the 20 km s^{-1} cloud, one of the massive molecular clouds in the CMZ.

The main results are:

- Various molecular lines are detected with the SMA and VLA observations, most of which are widespread and not always spatially coincident with the dense cores traced by dust emission. Analysis based on 2D cross-correlations between the dust and spectral line emission suggests that the CH_3OH , SO , and HNCO lines are best spatially correlated with compact dust emission from dense cores, which may suggest connections between the excitation of these lines and star formation in the dense cores.
- The line ratios between the ‘slow shock tracers’ (CH_3OH , SO , and HNCO) and the ‘fast shock tracer’ SiO show clear enhancement toward the compact dust emission, indicating the presence of slow shocks or hot molecular cores in these regions.
- Using multiple transitions of H_2CO and NH_3 , we estimate gas kinetic temperatures at ~ 0.1 -pc scales under non-LTE conditions. Temperatures derived from NH_3 lines are $\gtrsim 2$ times higher than those from H_2CO lines in several regions, which may suggest two gas components, while toward a dense core C4-P1 temperatures from H_2CO is higher, which may suggest internal heating. The high angular resolution data reveal high temperatures of > 50 K, and at some positions > 200 K at 0.1-pc scales, which are smeared to 50–100 K in lower angular resolution observations.
- Comparisons between kinetic temperatures and linewidths, as well as between kinetic temperatures and maser luminosities suggest no strong correlations. However, direct evidence of shock heating is found based on the high-angular-resolution

temperature maps, with evidence of shocks from the SiO emission. Several likely protostellar heated dense cores are also discussed.

In summary, our observations reveal two potential impacts of turbulence and star formation on the molecular gas environment at 0.1-pc scales in the 20 km s^{-1} cloud. First, the two factors may affect the chemical composition of the molecular gas. This is supported by widespread SiO emission in the cloud, which is likely related to fast shocks, as well as spatial correlation and enhancement of $\text{CH}_3\text{OH}/\text{HNCO}/\text{SO}$ emission toward compact dust emission from dense cores, which is likely related to slow shocks or embedded high-mass star formation. Second, the two factors may heat the molecular gas. Candidate shock heated regions of 0.1-pc scales and > 200 K temperatures are found throughout the cloud, while signatures of localized heating by embedded star formation are found in several likely internally heated dense cores. Such high-angular-resolution spectral line observations have been proved to be powerful in understanding gas properties in the complex environment in the CMZ. Future observations using ALMA that provide better spectral line sensitivity will be important for the study of star formation and dense gas in the CMZ clouds.

We thank the anonymous referee for a constructive review. We thank Simon Radford and William Tan for help with the CSO observation and data reduction, and Junhao Liu for helpful discussions on RADEX modelling. XL acknowledges the support of a Smithsonian Predoctoral Fellowship and the program A for outstanding PhD candidate of Nanjing University. JMDK gratefully acknowledges support in the form of an Emmy Noether Research Group from the Deutsche Forschungsgemeinschaft (DFG), grant number KR4801/1-1. CB is supported by the National Science Foundation under Award No. 1602583. ZYZ acknowledges support from the European Research Council in the form of the Advanced Investigator Programme, 321302, COSMICISM. This research made use of Astropy, a community-developed core Python package for Astronomy ([Astropy Collaboration et al. 2013](#)), and NASA’s Astrophysics Data System. This material is based upon work at the Caltech Submillimeter Observatory, which was operated by the California Institute of Technology. This publication is also based on data acquired with the Atacama Pathfinder Experiment (APEX). APEX is a collaboration between the Max-Planck-Institut für Radioastronomie, the European Southern Observatory, and the Onsala Space Observatory.

Facilities: SMA, VLA, CSO, APEX, GBT

Software: CASA, MIRIAD, MIR, GILDAS/CLASS, Astropy (Astropy Collaboration et al. 2013), RADEX (van der Tak et al. 2007), myRadex, correl_images.pro

REFERENCES

- Ao, Y., Henkel, C., Menten, K. M., et al. 2013, *A&A*, 550, A135
- Araya, E., Hofner, P., Kurtz, S., Bronfman, L., & DeDeo, S. 2005, *ApJS*, 157, 279
- Astropy Collaboration, Robitaille, T. P., Tollerud, E. J., et al. 2013, *A&A*, 558, A33
- Bachiller, R., & Pérez Gutiérrez, M. 1997, *ApJL*, 487, L93
- Barnes, A. L., Longmore, S. N., Battersby, C. D., et al. 2017, *MNRAS* submitted
- Coil, A. L., & Ho, P. T. P. 1999, *ApJ*, 513, 752
- Danby, G., Flower, D. R., Valiron, P., Schilke, P., & Walmsley, C. M. 1988, *MNRAS*, 235, 229
- Draine, B. T. 2003, *ARA&A*, 41, 241
- Ferrière, K. 2012, *A&A*, 540, A50
- Ferrière, K., Gillard, W., & Jean, P. 2007, *A&A*, 467, 611
- Garay, G., Mardones, D., & Rodríguez, L. F. 2000, *ApJ*, 545, 861
- Garrod, R. T., & Herbst, E. 2006, *A&A*, 457, 927
- Ginsburg, A., Glenn, J., Rosolowsky, E., et al. 2013, *ApJS*, 208, 14
- Ginsburg, A., Henkel, C., Ao, Y., et al. 2016, *A&A*, 586, A50
- Guesten, R., & Downes, D. 1983, *A&A*, 117, 343
- Guillet, V., Jones, A. P., & Pineau Des Forêts, G. 2009, *A&A*, 497, 145
- Harju, J., Walmsley, C. M., & Wouterloot, J. G. A. 1993, *A&AS*, 98, 51
- Henshaw, J. D., Longmore, S. N., Kruijssen, J. M. D., et al. 2016, *MNRAS*, 457, 2675
- Ho, P. T. P., Jackson, J. M., Barrett, A. H., & Armstrong, J. T. 1985, *ApJ*, 288, 575
- Ho, P. T. P., Moran, J. M., & Lo, K. Y. 2004, *ApJL*, 616, L1
- Ho, P. T. P., & Townes, C. H. 1983, *ARA&A*, 21, 239
- Immer, K., Kauffmann, J., Pillai, T., Ginsburg, A., & Menten, K. M. 2016, *A&A*, 595, A94
- Immer, K., Menten, K. M., Schuller, F., & Lis, D. C. 2012, *A&A*, 548, A120
- Jiménez-Serra, I., Caselli, P., Tan, J. C., et al. 2010, *MNRAS*, 406, 187
- Johnston, K. G., Beuther, H., Linz, H., et al. 2014, *A&A*, 568, A56
- Jones, P. A., Burton, M. G., Cunningham, M. R., et al. 2012, *MNRAS*, 419, 2961
- Kauffmann, J., Bertoldi, F., Bourke, T. L., Evans, II, N. J., & Lee, C. W. 2008, *A&A*, 487, 993
- Kauffmann, J., Pillai, T., & Zhang, Q. 2013, *ApJL*, 765, L35
- Kauffmann, J., Pillai, T., Zhang, Q., et al. 2016, *A&A* accepted, arXiv:1610.03499
- Kelly, G., Viti, S., García-Burillo, S., et al. 2017, *A&A*, 597, A11
- Kennicutt, R. C., & Evans, N. J. 2012, *ARA&A*, 50, 531
- Kennicutt, Jr., R. C. 1998, *ApJ*, 498, 541
- Krieger, N., Ott, J., Walter, F., et al. 2016, *ArXiv e-prints*, arXiv:1610.01615
- Kruijssen, J. M. D., Dale, J. E., & Longmore, S. N. 2015, *MNRAS*, 447, 1059
- Kruijssen, J. M. D., & Longmore, S. N. 2013, *MNRAS*, 435, 2598
- Kruijssen, J. M. D., Longmore, S. N., Elmegreen, B. G., et al. 2014, *MNRAS*, 440, 3370
- Krumholz, M. R., & Kruijssen, J. M. D. 2015, *MNRAS*, 453, 739
- Krumholz, M. R., Kruijssen, J. M. D., & Crocker, R. M. 2017, *MNRAS*, 466, 1213
- Lis, D. C., Menten, K. M., Serabyn, E., & Zylka, R. 1994, *ApJL*, 423, L39
- Liu, H. B., Ho, P. T. P., Wright, M. C. H., et al. 2013, *ApJ*, 770, 44
- Longmore, S. N., Pillai, T., Keto, E., Zhang, Q., & Qiu, K. 2011, *ApJ*, 726, 97
- Longmore, S. N., Bally, J., Testi, L., et al. 2013, *MNRAS*, 429, 987
- Lu, X., Zhang, Q., Kauffmann, J., et al. 2015, *ApJL*, 814, L18
- Lu, X., Zhang, Q., Liu, H. B., Wang, J., & Gu, Q. 2014, *ApJ*, 790, 84
- Mangum, J. G., & Wootten, A. 1993, *ApJS*, 89, 123
- Martín-Pintado, J., de Vicente, P., Fuente, A., & Planesas, P. 1997, *ApJL*, 482, L45
- Martín-Pintado, J., Rizzo, J. R., de Vicente, P., Rodríguez-Fernández, N. J., & Fuente, A. 2001, *ApJL*, 548, L65
- McMullin, J. P., Waters, B., Schiebel, D., Young, W., & Golap, K. 2007, in *ASP Conf. Ser.*, Vol. 376, *Astronomical Data Analysis Software and Systems XVI*, ed. R. A. Shaw, F. Hill, & D. J. Bell (San Francisco, CA: ASP), 127
- Mezger, P. G., Smith, L. F., & Churchwell, E. 1974, *A&A*, 32, 269
- Mills, E. A. C., Butterfield, N., Ludovici, D. A., et al. 2015, *ApJ*, 805, 72
- Mills, E. A. C., & Morris, M. R. 2013, *ApJ*, 772, 105
- Minh, Y. C., Liu, H. B., Ho, P. T. P., et al. 2013, *ApJ*, 773, 31
- Molinari, S., Bally, J., Noriega-Crespo, A., et al. 2011, *ApJL*, 735, L33
- Morris, M., & Serabyn, E. 1996, *ARA&A*, 34, 645
- Oka, T., Hasegawa, T., Sato, F., Tsuboi, M., & Miyazaki, A. 1998, *ApJS*, 118, 455
- Oka, T., Onodera, Y., Nagai, M., et al. 2012, *ApJS*, 201, 14
- Ott, J., Weiß, A., Staveley-Smith, L., Henkel, C., & Meier, D. S. 2014, *ApJ*, 785, 55
- Palla, F., Cesaroni, R., Brand, J., et al. 1993, *A&A*, 280, 599
- Panagia, N. 1973, *AJ*, 78, 929
- Perley, R. A. 1999, in *Astronomical Society of the Pacific Conference Series*, Vol. 180, *Synthesis Imaging in Radio Astronomy II*, ed. G. B. Taylor, C. L. Carilli, & R. A. Perley, 275
- Rathborne, J. M., Longmore, S. N., Jackson, J. M., et al. 2014a, *ApJ*, 786, 140
- . 2014b, *ApJL*, 795, L25
- . 2015, *ApJ*, 802, 125
- Reid, M. J., Menten, K. M., Brunthaler, A., et al. 2014, *ApJ*, 783, 130
- Requena-Torres, M. A., Martín-Pintado, J., Martín, S., & Morris, M. R. 2008, *ApJ*, 672, 352
- Requena-Torres, M. A., Martín-Pintado, J., Rodríguez-Franco, A., et al. 2006, *A&A*, 455, 971
- Riquelme, D., Bronfman, L., Mauersberger, R., May, J., & Wilson, T. L. 2010, *A&A*, 523, A45
- Rodríguez, L. F., & Zapata, L. A. 2013, *ApJL*, 767, L13
- Rodríguez-Fernández, N. J., Combes, F., Martín-Pintado, J., Wilson, T. L., & Apponi, A. 2006, *A&A*, 455, 963
- Rodríguez-Fernández, N. J., Tafalla, M., Gueth, F., & Bachiller, R. 2010, *A&A*, 516, A98
- Sault, R. J., Teuben, P. J., & Wright, M. C. H. 1995, in *ASP Conf. Ser.*, Vol. 77, *Astronomical Data Analysis Software and Systems IV*, ed. R. A. Shaw, H. E. Payne, & J. J. E. Hayes (San Francisco, CA: ASP), 433

Shetty, R., Beaumont, C. N., Burton, M. G., Kelly, B. C., & Klessen, R. S. 2012, MNRAS, 425, 720
 Shirley, Y. L. 2015, PASP, 127, 299
 Sridharan, T. K., Beuther, H., Schilke, P., Menten, K. M., & Wyrowski, F. 2002, ApJ, 566, 931
 Stolovy, S., Ramirez, S., Arendt, R. G., et al. 2006, Journal of Physics Conference Series, 54, 176
 Tsuboi, M., Tadaki, K.-I., Miyazaki, A., & Handa, T. 2011, PASJ, 63, 763
 Usero, A., García-Burillo, S., Martín-Pintado, J., Fuente, A., & Neri, R. 2006, A&A, 448, 457
 Vacca, W. D., Garmany, C. D., & Shull, J. M. 1996, ApJ, 460, 914

van der Tak, F. F. S., Black, J. H., Schöier, F. L., Jansen, D. J., & van Dishoeck, E. F. 2007, A&A, 468, 627
 Walmsley, C. M., & Ungerechts, H. 1983, A&A, 122, 164
 Wiesenfeld, L., & Faure, A. 2013, MNRAS, 432, 2573
 Wright, M. C. H., Coil, A. L., McGary, R. S., Ho, P. T. P., & Harris, A. I. 2001, ApJ, 551, 254
 Yusef-Zadeh, F., Hewitt, J. W., Arendt, R. G., et al. 2009, ApJ, 702, 178
 Zhang, Z.-Y., Henkel, C., Gao, Y., et al. 2014, A&A, 568, A122

APPENDIX

A. ESTIMATE OF KINETIC TEMPERATURES USING RADEX

After running myRadex with the grids described in Section 3.5, we derived the likelihood of the observed H₂CO 3_{0,3}-2_{0,2} peak brightness temperatures being reproduced at given gas temperatures, H₂ densities and several typical column densities. The grey shades in Figure A1 show the normalized likelihood for the observed H₂CO transitions towards the C4-P1 dense core in the SMA+APEX data at a fixed column density of 10²³ cm⁻². Details can be found in Zhang et al. (2014). As pointed out by Ao et al. (2013), the line ratios between H₂CO 3_{2,2}-2_{2,1} and 3_{0,3}-2_{0,2} are more sensitive to gas densities therefore are not as good thermometers as the line ratios between H₂CO 3_{2,1}-2_{2,0} and 3_{0,3}-2_{0,2}. In Figure A1 we plot the latter line ratios from the models as black contours, which indeed are almost independent of gas densities while sensitive to kinetic temperatures.

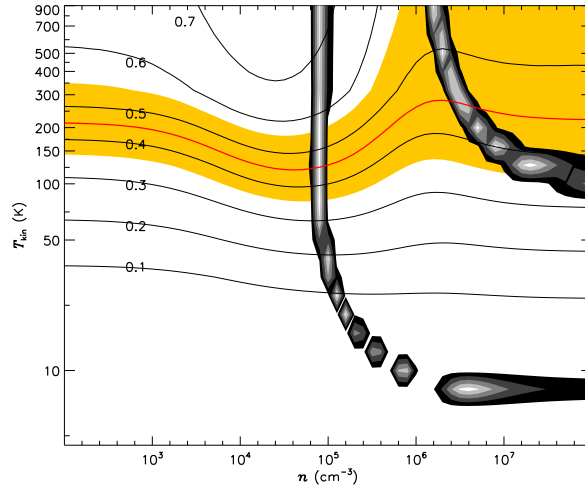


Figure A1. RADEX modelling of SMA+APEX H₂CO lines toward the C4-P1 dense core. The grey shades show the normalized likelihood of the observed H₂CO 3_{0,3}-2_{0,2} peak brightness temperatures being reproduced in RADEX, with values from 0.1 to 0.9 in steps of 0.2 from the darkest to the brightest. The observed H₂CO 3_{2,1}-2_{2,0} and 3_{0,3}-2_{0,2} peak intensity ratio is highlighted with a red contour, while the yellow shade around it represents the 1 σ error of the line ratio due to the observational uncertainty of 0.1 Jy beam⁻¹ in the line intensities.

For the H₂CO lines toward the C4-P1 dense core in the SMA+APEX data, the peak brightness temperatures of the H₂CO 3_{2,1}-2_{2,0} and 3_{0,3}-2_{0,2} transitions are 1.13 K and 2.51 K, which leads to a ratio of 0.45. Therefore, the intersection between the ratio=0.45 contour (highlighted in red in Figure A1) and the highest likelihood for H₂CO brightness temperatures (brightest grey shades in Figure A1) represent the most likely gas temperatures and H₂ densities that can simultaneously reproduce the observed H₂CO 3_{0,3}-2_{0,2} intensities and the observed line ratios. Hence the estimated gas temperature is \sim 120 K and the estimated gas density is \sim 10⁵ cm⁻³. The estimated temperature and density depend on the assumed column density and H₂CO abundance. For example, varying the abundance from 10⁻⁹ to 2 \times 10⁻⁹ while keeping the other conditions unchanged will bring the estimated temperature to 110 K and the estimated density to 4 \times 10⁴ cm⁻³. In addition, the optical depth of the H₂CO 3_{0,3}-2_{0,2} transition derived at the same time is 0.98, which suggests the H₂CO line is getting optically thick therefore sensitivity to temperatures is

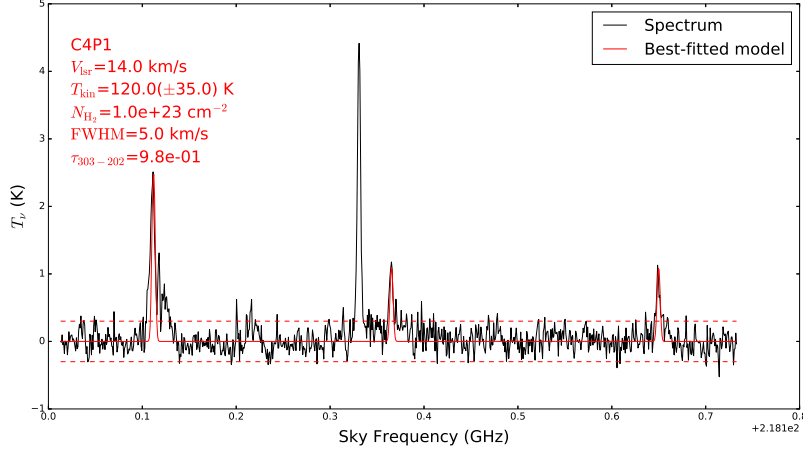


Figure A2. The observed SMA+APEX H_2CO spectrum toward C4-P1, shown in black curve, and the expected spectrum from the RADEX modelling, shown in red curve. The input parameters of the model spectrum are shown in the figure. The horizontal dashed lines represent $\pm 3\sigma$ levels.

disappearing (Ginsburg et al. 2016). The rms of observed H_2CO line intensities also bring in an uncertainty of 30%, as shown in Figure A1. Taking all these factors into account, we assume an uncertainty of 0.15 dex (40%) for the kinetic temperatures. Note that the collision rates we were using were extrapolated above 300 K (Wiesenfeld & Faure 2013; discussions in Ginsburg et al. 2016), therefore temperatures >300 K are not reliable (they are derived when large H_2CO line ratios are found due to optically thick emission therefore have large uncertainties themselves anyway).

To examine the quality of the modelling, in Figure A2 we plot the H_2CO spectrum extracted towards C4-P1 in the SMA+APEX data and the model constructed with the parameters estimated above. The model reproduces the observed H_2CO spectrum well. The blue-shifted ‘line wings’ seen in H_2CO $3_{0,3}-2_{0,2}$ and $3_{2,2}-2_{2,1}$ transitions could be a different velocity component.

In Section 3.5 we have noticed that the H_2CO $3_{2,1}-2_{2,0}$ to $3_{0,3}-2_{0,2}$ line ratios are sensitive to kinetic temperatures, but not so to H_2 densities or column densities. We limited H_2 densities within $10^4-10^5 \text{ cm}^{-3}$, which are the range we obtained in RADEX models, and column densities within $5 \times 10^{22}-5 \times 10^{23} \text{ cm}^{-2}$, which are from *Herschel* observations. Then we plot the estimated temperatures against the H_2CO line ratios in Figure A3. A least-square fit to the line ratio– $\log(T_{\text{kin}})$ relation between $T_{\text{kin}} = 30-300$ K led to the relation shown in Figure A3. A similar relation has been derived in Ginsburg et al. (2016) (see their Figure 6). In Section 3.5 we used this relation to directly convert observed H_2CO line ratios to kinetic temperatures.

Then we applied the above analyses to the VLA NH_3 (2, 2) and (4, 4) spectra. In Figure A4, we plot the modelling result for the NH_3 lines toward the C4-P1 dense cores at a fixed column density of 10^{23} cm^{-2} , but using an NH_3

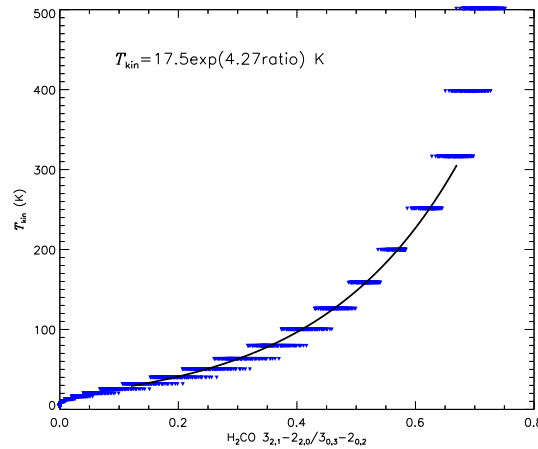


Figure A3. The H_2CO $3_{2,1}-2_{2,0}/3_{0,3}-2_{0,2}$ line ratios and the kinetic temperatures from RADEX models. At each temperature, we took the line ratios from models with several H_2 densities between 10^4 and 10^5 cm^{-3} , and column densities between 5×10^{22} and $5 \times 10^{23} \text{ cm}^{-2}$. The solid line is a least-square fit to the ratio– $\log(T_{\text{kin}})$ relation between $T_{\text{kin}} = 30-300$ K.

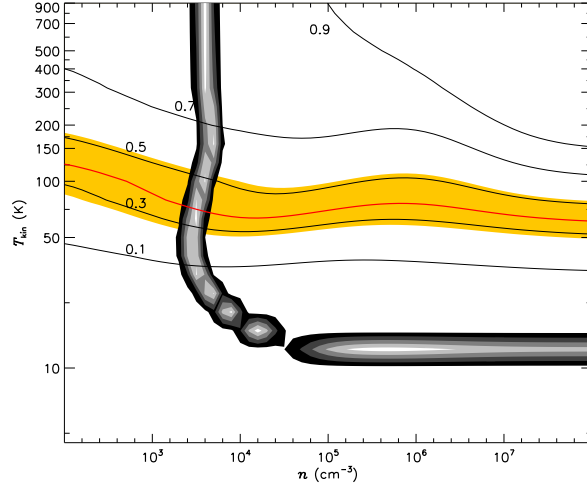


Figure A4. RADEX modelling of VLA NH_3 lines toward the C4-P1 dense core. The shaded regions show the normalized likelihood of the observed NH_3 (2, 2) peak brightness temperatures being reproduced in RADEX, with values from 0.1 to 0.9 in steps of 0.2 from the darkest to the brightest. The observed NH_3 (4, 4) and (2, 2) line ratio is highlighted with a red contour, while the yellow shaded region represents the 1σ error of the line ratio due to the observational uncertainty of 2 mJy beam^{-1} in the line intensities.

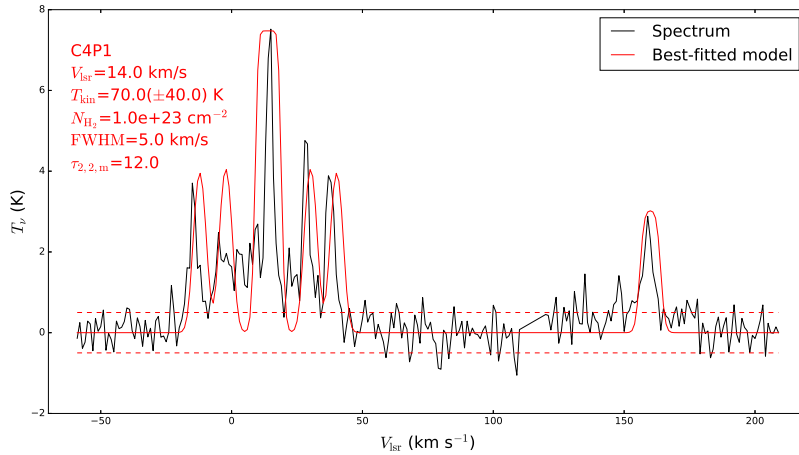


Figure A5. The observed VLA+GBT NH_3 (2, 2) and (4, 4) spectra toward C4-P1, shown in black curve, and the expected spectra from the RADEX modelling, shown in red curve. Note that the NH_3 (4, 4) spectrum has been horizontally shifted by $+150 \text{ km s}^{-1}$. The input parameters of the model spectra are shown in the figure. The horizontal dashed lines represent $\pm 3\sigma$ levels.

abundance of 1.8×10^{-7} instead of 3×10^{-8} in order to fit the hyperfine structures of NH_3 (2, 2). The black contours show the ratios between NH_3 (4, 4) and (2, 2) peak brightness temperatures from the models and the grey shades show the normalized likelihood of the observed NH_3 (2, 2) peak brightness temperature (6.42 K) being reproduced in the models. The observed NH_3 (4, 4)/(2, 2) line ratio in C4-P1 is 0.34. Therefore the estimated kinetic temperature is $\sim 70 \text{ K}$ and the estimated density is $\sim 3 \times 10^3 \text{ cm}^{-3}$. The optical depth of the NH_3 (2, 2) main hyperfine component derived at the same time is 12. For the same reason of extrapolated collision rates (Danby et al. 1988), temperatures above 300 K are not reliable either. Note that if we use an NH_3 abundance of 3×10^{-8} as mentioned in Section 3.5, the estimated temperature would be $\sim 100 \text{ K}$ but the model could not fit the NH_3 (2, 2) satellite components.

In Figure A5, we also compare the NH_3 spectra extracted towards C4-P1 in the VLA+GBT data with the model constructed with the parameters estimated above. The model can reproduce intensities of the observed NH_3 (2, 2) and (4, 4) main hyperfine components, as well as the satellite hyperfine components of NH_3 (2, 2). However, due to the large optical depth, the model lines are much broader than observed. It is possible that multiple optically thick components with small filling factors exist, which lead to the large satellite-to-main line ratio in NH_3 (2, 2), but do not produce broad lines because of their smaller intrinsic linewidths.

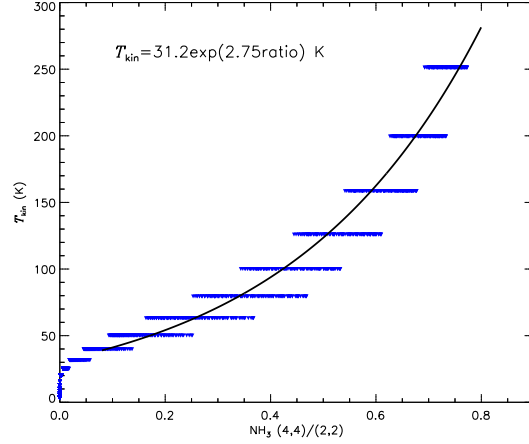


Figure A6. The NH_3 (4, 4)/(2, 2) line ratios and the kinetic temperatures from RADEX models. At each temperature, we took the line ratios from models with H_2 densities between 10^4 and 10^5 cm^{-3} , and column densities between 5×10^{22} and $5 \times 10^{23} \text{ cm}^{-2}$. The solid line is a least-square fit to the ratio- $\log(T_{\text{kin}})$ relation between $T_{\text{kin}} = 30\text{--}300 \text{ K}$.

The strong NH_3 (2, 2) satellite components shown in [Figure A5](#) are not universal in the 20 km s^{-1} cloud. We only find such spectra toward several massive dense cores, including C4-P1 and C5-P1. For most of the area in the cloud, the NH_3 (2, 2) satellite components are weak, suggesting optically thin emission, and the assumed NH_3 abundance of 3×10^{-8} can fit the observed spectra well. Therefore, we continued to use the abundance of 3×10^{-8} , but it must be kept in mind that in several dense cores a higher abundance is likely and resulting temperatures can be lower by 30%. Again the rms of observed NH_3 line intensities bring in an uncertainty of 30% as shown in [Figure A4](#). Overall, we assume an uncertainty of 0.16 dex (45%) for the kinetic temperatures.

In [Figure A6](#), we plot the estimated kinetic temperatures against the NH_3 line ratios from the models, within the same ranges of H_2 densities and column densities as for the H_2CO and an NH_3 abundance of 3×10^{-8} . Then a least-square fit between $T_{\text{kin}} = 30\text{--}300 \text{ K}$ led to the relation shown in the figure, with which we obtained the kinetic temperature map in [Section 3.5](#).